Theory and Performance of Tesla Turbines

by

Vincent Domenic Romanin

A dissertation submitted in partial satisfaction of the
requirements for the degree of
Doctor of Philosophy

in

Engineering - Mechanical Engineering

in the

Graduate Division

of the

University of California, Berkeley

Committee in charge:

Professor Van P. Carey, Chair
Professor Ömer Savaş
Associate Professor Michel Maharbiz

Fall 2012

Theory and Performance of Tesla Turbines

Abstract

Theory and Performance of Tesla Turbines

by

Vincent Domenic Romanin

Doctor of Philosophy in Engineering - Mechanical Engineering

University of California, Berkeley

Professor Van P. Carey, Chair

This document summarizes the development of an integral perturbation solution of the equations governing momentum transport in microchannels between disks of multiple-disk drag turbines such as the Tesla turbine. This analysis allows a parametric study of turbine performance based on several nondimensional parameters. The results of this analysis are then compared to two sets of test data published in previous work and by other projects. The results are further compared to Computational Fluid Dynamics (CFD) simulations. Finally, expected performance and potential applications of these devices are discussed in light of the results developed.

Analysis of this type of flow problem is a key element in the optimal design of Tesla drag-type turbines for geothermal, waste heat, energy harvesting, or solar alternative energy applications. In multiple-disk turbines, high speed flow enters tangentially at the outer radius of cylindrical microchannels formed by closely spaced parallel disks, spiraling through the channel to an exhaust at a small radius or at the center of the disk. Previous investigations have generally developed models based on simplifying idealizations of the flow in these circumstances. Here, beginning with the momentum and continuity equations for incompressible and steady flow in cylindrical coordinates, an integral solution scheme is developed that leads to a dimensionless perturbation series solution that retains the full complement of momentum and viscous effects to consistent levels of approximation in the series solution. This more rigorous approach indicates all dimensionless parameters that affect flow and transport, and allows a direct assessment of the relative importance of viscous, pressure, and momentum effects in different directions in the flow. The resulting lowest-order equations are solved explicitly and higher order terms in the series solutions are determined numerically.

Enhancement of rotor drag in this type of turbine enhances energy conversion efficiency. A modified version of the integral perturbation analysis is presented that incorporates the effects of enhanced drag due to surface microstructuring. Results of the model analysis for smooth disk walls are shown to agree well with experimental performance data for two prototype Tesla turbines, and predictions of performance models developed in earlier inves-

tigations. Specifically, experimental efficiencies corelate well with those predicted by the integral perturbation solution, deviating by an average of 29% and a maximum of 52%. Model predictions indicate that enhancement of disk drag by strategic microstructuring of the disk surfaces can significantly increase turbine efficiency. Exploratory calculations with the model indicate that turbine efficiencies exceeding 75% can be achieved by designing for optimal ranges of the governing dimensionless parameters.

The same parametric trends in performance are compared to test data for a micro-scale Tesla turbine with water as a working fluid. Experimental efficiencies again correlate well with those predicted by the integral perturbation solution. Exerimental efficiencies show a mean deviation of 52% with efficiencies predicted by the model, and a max deviation of 65%. A Computational Fluid Dynamics (CFD) model is then compared to both the analytical and experimental turbine efficiencies. The CFD solutions of the flow field are then used to help reconcile areas where the analytical predictions do not match experimental data. CFD predicted efficiencies match the efficiencies predicted by the integral perturbation solution very closely, deviating by an average of only 18%.

Based on the results of the CFD simulations and experimental data, conclusions are made about the validity of the integral perturbation solution. The model accurately predicts the flow inside the rotor, but a better treatment of the flow in the inlet to the turbine is necessary. Despite this, the integral perturbation solution is shown to be capable of directing high efficiency turbine design, and design strategies and parameter ranges that result in high efficiency devices are outlined.

To my Mother and Father, the two most influential engineering mentors I have had. This work would not have been possible without the moral and academic support of the Energy and Information Technologies Laboratory, including but not limited to my advisor Professor Van P. Carey and my colleagues Yu Gan, Sara Beaini, Kenneth Armijo, Jorge Padilla, David Lettieri, Michael Toulouse, and Maritza Ruiz. I am fortunate to have worked with some of the most intelligent and supportive engineers in the field of heat transfer. I am also indebted to all the faculty and staff of the University of California, Berkeley Mechanical Engineering department, especially the student services office and the student machine shop staff, whose support has been instrumental to my research and studies.

Contents

List of Figures

List of Tables

Nomenclature

$\bar{v}$	Mean (axially averaged) velocity, page 20
Δh_{isen}	Isentropic enthalpy drop, page 26
$\dot{\mathcal{W}}$	Shaft power, page 14
$\dot{m}_c$	Mass flow rate per disk gap, page 22
η_i	Isentropic efficiency of the turbine as predicted by the integral perturbation solution of flow through the rotor, page 26
η_{CFD}	Isentropic efficiency of the turbine as predicted by ANSYS, page 37
η_{exp}	Experimental turbine efficiency, page 15
$\eta_{i,inc}$	Isentropic efficiency of the turbine as predicted by the integral perturbation solution of flow through the rotor, incompressible nozzle flow, page 35
η_{noz}	Isentropic nozzle efficiency, page 18
η_{rm}	Efficiency of the rotor, page 26
γ	Heat capacity ratio (c_p/c_v), page 17
$\hat{P}$	Dimensionless pressure, page 23
$\hat{P}'$	Derivative of $\hat{P}$ with respect to ξ ($d\hat{P}/d\xi$), page 23
$\hat{P}_0, \hat{P}_1, ...$	0th order ($*\varepsilon^0$), 1st order($*\varepsilon^1$), etc. pressure terms, page 24
$\hat{v}$	Mean velocity difference ($= \bar{v} - U$), page 20
$\hat{W}_i$	Dimensionless velocity difference at the turbine inner radius, page 26
$\hat{W}$	Dimensionless relative velocity difference, page 23
$\hat{W}', \hat{W}''$	First and second derivative of $\hat{W}$ with respect to ξ ($d\hat{W}/d\xi, d^2\hat{W}/d\xi^2$), page 23

$\hat{W}_0, \hat{W}_1, ...$	0th order ($*\varepsilon^0$), 1st order($*\varepsilon^1$), etc. velocity terms, page 24
$\hat{W}_o$	Dimensionless velocity difference at the turbine outer radius, page 23
$\hat{W}_{0,r_o}$	0th order dimensionless velocity difference at the turbine outer radius, page 24
$\mathbf{v}$	Velocity vector, page 18
Po	Poiseuille number ($= f \cdot \mathrm{Re}$), page 21
Re_c	Reynolds number, page 20
Re_m^*	Modified Reynolds number, page 23
μ	Viscocity, page 20
ν	Kinematic viscocity, page 19
ω	Angular velocity of the rotor, page 25
$\phi(z)$	Dimensionless velocity profile, page 20
ρ	Density, page 19
τ	Torque, page 14
τ_w	Wall shear stress, page 20
θ	Azimuthal coordinate, page 19
ε	Disk gap aspect ratio ($= D_H/r_o$), page 23
ξ	Dimensionless radial coordinate, page 23
a_t	Speed of sound at nozzle throat, page 18
b	Gap distance between disks, page 20
c_p	Specific heat capacity at constant pressure, page 18
D_H	Hydraulic diameter, page 3
f	Friction factor, page 20
F_{Po}	Drag enhancement number ($= Po/24$), page 21
J	Moment of inertia of the rotor, page 14
M_o	Rotor tip Mach number ($= U_o/\sqrt{\gamma R T_t}$), page 25

n	Velocity profile modifier, page 20
P	Pressure, page 19
P^*	Dimensionless pressure for incompressible nozzle flow, page 35
P_o	Pressure at the turbine outer radius, page 17
P_o	Pressure at the turbine outer radius, page 23
P_{nt}	Total pressure upstream of the nozzle, page 17
R	Ideal gas constant, page 18
r	Radial coordinate, page 19
r_o, r_i	Outer and inner radius of turbine disk, respectively, page 3
T_t	Gas temperature at nozzle throat for choked flow, page 18
T_{nt}	Total temperature upstream of the nozzle, page 18
U	Disk velocity, page 20
U_o, U_i	Disk speed at the turbine outer and inner radius, respectively, page 23
v_θ	Tangential component of fluid velocity, page 17
v_r	Radial component of fluid velocity, page 19
v_z	Axial component of fluid velocity, page 19
$v_{o,c}$	Nozzle exit velocity for choked flow (of an ideal gas), page 18
$v_{o,i}$	Isentropic nozzle exit velocity for choked flow, page 18
V_{ro}	Dimensionless radial velocity at the turbine outer radius, page 23
z	Axial coordinate, page 19

Acknowledgments

Support for this research by the UC Center for Information Technology Research in the Interest of Society (CITRIS) is gratefully acknowledged.

Chapter 1

Introduction

1.1 Motivation

Sub-Megawatt turbines, also known as microturbines, are integral to the recently growing fields of Combined Heat and Power (CHP), energy harvesting, and small scale power generation. The demands and design requirements of microturbines are different from megawatt and larger turbines, due to manufacturing limitations and the varying demands of specific applications. Properties of viscous flow turbines, like the Tesla turbine, may be conducive to solving some of the specific challenges in this design space. This study aims to provide a foundation for designing Tesla turbines with power output ranging from ∼1 kW down to ∼1 microwatt.

Kilowatt scale power generation has applications in Combined Heat and Power (CHP) power plants, waste heat recovery, geothermal power, and distributed-scale electricity generation. The primary advantage of CHP systems is that the waste heat from the power cycle is generated at the point of end use, and can be utilized for industrial process heating, space heating, or water heating. The international energy agency (IEA) has identified CHP as an important part of greenhouse gas reduction strategies, and suggests policy changes that may encourage development of these systems. The IEA also stated that CHP is economical in that it does not need governmental economic incentives to be cost effective [3]. Since CHP power plants are deployed at the end-use location of the generated heat, they are typically small, on the order of 1 kW when the heat is being used in a singe residential unit, up to about 1 GW when heat is being distributed on a citywide scale. While traditional radial turbines can be used in large-scale CHP, smaller scale CHP plants require highly efficient expanders to be economical. Similarly, waste heat streams from industrial processes, and geothermal heat streams represent potential applications of microturbines. The efficiency of current microturbine technologies in the kilowatt size range vary depending on the type of device, type of fuel, and application, but typical efficiencies are in the 20 - 40% range ([6], [16]). If Tesla turbines can be designed with comparable efficiencies, they can compete well with other turbine technologies since Tesla turbines can be made comparatively cheaply.

Watt scale and smaller turbines have also been of interest recently. Liquid hydrocarbon fuels have energy densities about 100 times greater than current battery technology, so turbines with as low as 10% electrical efficiency can still have power densities an order of magnitude higher than batteries ([8], [7]). This type of power plant could be particularly advantageous to aerial vehicles in which a lightweight powerplant is important and military applications where small devices must be carried and weight is critical. Fernandez-Pello provides an overview of combustion-based micropower generation in [8], and states that challenges faced by scaling down include overcoming viscous forces due to low Reynolds numbers in microchannel flow, combustion at small size scales, and fabrication.

A final application for sub-watt scale turbines is remote sensing applications where energy must be harvested from the environment. Many options are available for mili and micro-watt power generation, including but not limited to, photovoltaics, batteries, energy harvesting from vibration or motion via a peizoelectric or magnetic induction device, and ultra-small turbines like the Tesla turbine. At the small power requirements of many sensors, the primary concern for energy harvesting is not efficiency but durability, cost, and reliability. In applications where a fluid flow pressure head is a readily available power source, and where other power sources are scarce, Tesla turbines may provide a low cost and reliable solution to power generation, especially since the feasibility of more complex expander devices drops off significantly at ultra-small sizes [5].

The common thread in the diversity of applications listed is that a turbine only needs to be moderately efficient (10% - 40%, depending on the application) to compete favorably with existing technologies, and that simplicity and cost can sometimes take precedence over efficiency. Tesla turbines provide a unique opportunity and a compelling case for small scale turbines for several reasons. First, the simplicity of Tesla turbines allows them to be manufactured at small scales cheaply and effectively, in contrast to bladed turbines. Epstein [7] Fu [9] and Fernandez-Pello [8] all cite manufacturing capabilities as limitations to manufacturing their respective turbine types at small scales. A second issue is that viscous forces become more important at small scales. Tesla turbines, in contrast to other devices, rely on viscous forces to transfer energy from the moving fluid to the rotor, and for this reason may actually benefit from scaling down to small sizes. These reasons provide a compelling case for investigating Tesla turbine technology for power plants ranging from 1 kW down to 1 microwatt.

Aside from applications for which Tesla turbines have already been examined, a thorough understand of Tesla turbine performance could illuminate additional opportunities for added efficiency in power cycles, energy extraction from waste heat streams or pressure heads, or new opportunities for energy generation. Because Tesla turbine technology is still a very immature technology, this study does not aim to investigate Tesla turbines for any specific application, but rather to provide a fundamental understanding of Tesla turbine operation, and to provide a framework for analyzing and optimizing the performance of these devices.

1.2 History of the Tesla Turbine

The Tesla turbine was patented in 1913 by Nikola Tesla [21]. Tesla argued in his patent that for high efficiency devices, changes in velocity and direction should be gradual. Tesla sought to design a device where the fluid was allowed to follow its natural path with minimal disturbance, both to increase efficiency and to reduce cost and complexity in the device. Already having patented the Tesla Pump, he outlined the principles behind Tesla turbine operation and contrasted the two devices in his patent [21].

Tesla also pointed out several important factors affecting performance, including that increasing size and speed increases the efficiency, as does decreasing the disk spacing (although at the cost of torque). He describes several advantages over traditional devices, including simplicity, low weight, low maintenance, low cost, reliability, and compactness. He mentions that centrifugal pressure gradients, increasing with the square of velocity, prevent the device from running away to high speeds and thus damaging the device.

Operating Principles

Multiple-disk Tesla-type drag turbines rely on a mechanism of energy transfer that is fundamentally different from most typical airfoil-bladed turbines or positive-displacement expanders. A schematic of the Tesla turbine can be found in Figure 1.1. The turbine rotor consists of several flat, parallel disks mounted on a shaft with a small gap between each disk; these gaps form the cylindrical microchannels through which momentum is transfered from the fluid to the rotor. Exhaust holes on each disk are placed as close to the center shaft as possible. A turbine casing surrounds the disks with a low pressure port near the exhaust holes in each disk, and with a high pressure nozzle positioned at the outer edges of the disks and pointed at the gaps between each disk. Flow from the nozzle enters the cylindrical microchannels at an outer radius r_o where $r_o \gg D_H$ (D_H is the hydraulic diameter of the microchannels). The flow enters the channels at a high speed and a direction nearly tangential to the outer circumference of the disks, and exits through an exhaust port at a much smaller inner radius r_i. Energy is transferred from the fluid to the rotor via the shear force at the microchannel walls. As the spiraling fluid loses energy, the angular momentum drops causing the fluid to drop in radius until it reaches the exhaust port at r_i. This process is shown in Figure 1.2.

Applications

Since its invention, the Tesla turbine has not had any significant commercial applications. The Tesla pump has, because of its ability to handle abrasive fluids, fluids with entrained solids, or other fluids that cannot be handled with traditional pumps, and because of their simple and robust operation. Similarly, Tesla turbines may find applications where the working fluid is incompatible with traditional turbomachinery, such as fluids with high viscosities, abrasives, solid particles, or two phase fluids. The reason for this is that the boundary layer

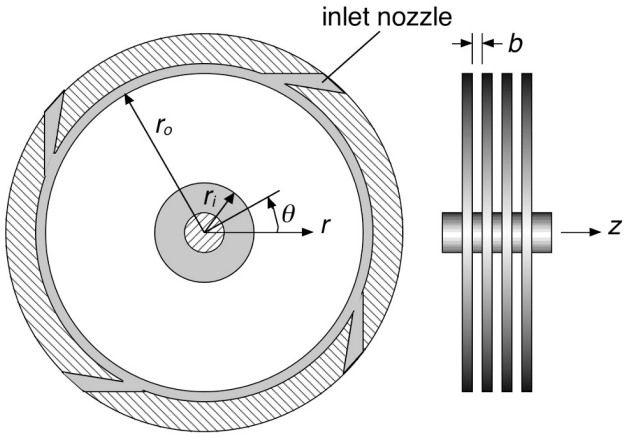

Figure 1.1: Schematic of a Tesla turbine.

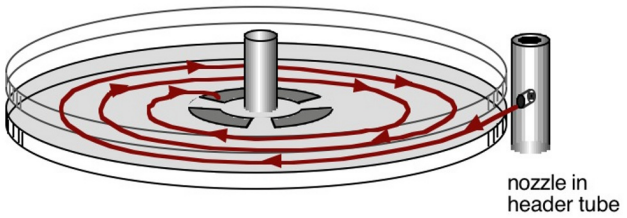

Figure 1.2: Schematic of flow through a Tesla turbine microchannel

near the disk wall has a small velocity, and a direction parallel to the surface, which precludes direct impingement of particles on the rotor.

Tesla turbines may also find utility where traditional turbines are prohibitively complex or costly to manufacture or maintenance. Tesla turbines may be manufactured with widely available machining technologies because the turbine does not require complex geometries like bladed turbines. Also, air leakage between the stationary casing and moving motive device does not occur in the Tesla turbine like it does in bladed and piston expander devices, so tight manufacturing tolerances are not required.

1.3 Background Research

Several authors have studied Tesla turbines in order to gain insight into their operation. In the 1960s, Rice[17] and Breiter et al.[1] conducted extensive analysis and testing of Tesla turbines. However, Rice did not directly compare experimental data to analytical results,

and lacked an analytical treatment of the friction factor. Breiter et al. provided a preliminary analysis of pumps only, and used a numerical solution of the energy and momentum equations. Hoya[12] and Guha[11] extensively tested sub-sonic and super-sonic nozzles with Tesla turbines, however their analysis was focused on experimental results and not an analytical treatment of the fluid mechanics that drive turbine performance. Krishnan [14] tested several mW-scale turbines, and reported a 36% efficiency for a 2 cc/sec flow rate with a 1 cm diameter rotor.

From a 1-D viscous incompressible turbine, Deam [5] analyzes the flow using the energy equation and concludes that the maximum turbine efficiency is 40%, due to exit losses and heat dissipation. In Deam's 1D analysis of linear viscous turbines, the exit velocity must be the same as the inlet velocity, which leads to a cost of about 33% of the efficiency. In a Tesla rotor, the exit velocity can be lower than the entrance velocity because of the cylindrical geometry, and for this reason the theoretical upper limit to efficiency is expected to be higher than 40%.

Carey[2] proposed an analytical treatment that allowed for a closed-form solution of the fluid mechanics equations in the flow in the rotor; however, Carey's model analysis invoked several idealizations that neglected viscous transport in the radial and tangential directions, and treated lateral viscous effects using a friction factor approach.

Romanin [19] applied Carey's [2] solution to flow through the rotor to test data for a 73 mm diameter turbine running compressed air. In this study, Romanin outlines several performance enhancement strategies based on the combination of test data and Carey's analytical solution to flow in the rotor, including decreasing disk spacing, increasing turbine speed, and increasing the number of disks (or decreasing the mass flow rate per disk). Romanin also raised issues concerning several of the assumptions made in Carey's analytical model, including the assumption that flow is axisymmetric when most Tesla devices use a discrete number of nozzles, and the lack of focus on nozzle design. The conclusions of this study motivated the present study, which aims to improve on the analytical treatment of flow in the rotor presented by Carey [2], to address issues of nozzle flow and non-axisymmetric rotor flow, to provide tools for predicting the pressure drop through the rotor, and to make further recommendations for Tesla turbine design and application.

The performance analyses in the previous investigations described above suggest that enhancement of rotor drag in this type of turbine generally enhances energy conversion efficiency. Information obtained in recent fundamental studies indicates that laminar flow drag can be strongly enhanced by strategic microstructuring of the wall surfaces in microchannels[13][4][10]. The conventional Moody diagram shows that for most channels, surface roughness has no effect on the friction factor for laminar flow in a duct. However, in micro-scale channels several physical near-surface effects can begin to become significant compared to the forces in the bulk flow. First, the Moody diagram only considers surface roughnesses up to 0.05, which is small enough not to have meaningful flow constriction effects. In microchannels, manufacturing techniques may often lead to surface roughnesses that comprise a larger fraction of the flow diameter. When the reduced flow area becomes small enough to affect flow velocity, the corresponding increase in wall sheer can become significant. Sec-

ondly, the size, shape, and frequency of surface roughness features can cause small areas of recirculation, downstream wakes, and other effects which may also impact the wall shear in ways that become increasingly important in smaller size channels, as the energy of the perturbations become relevant compared to the energy of the bulk flow.

In 2005, Kandlikar et. al[13] modified the traditional Moody diagram to account for surfaces with a relative roughness higher than 0.05, arguing that above this value flow constriction becomes important. Kandlikar proposes that the constricted diameter be simplified to be $D_{cf} = D_t - 2\varepsilon$, where ε is the roughness height, D_t is the base diameter, and D_{cf} is the constricted diameter. Using this formulation, the Moody diagram can be re-constructed to account for the constricted diameter, and can thus be used for channels with relative roughness larger than 5%. Kandlikar conducts experiments which match closely with this prediction, and significantly closer than the prediction of the classical Moody diagram. Kandlikar, however, only conducts experiments on one type of roughness element, and does not analyze the effect of the size, shape, and distribution of roughness elements, although he does propose a new set of parameters that could be used to further characterize the roughness patterns in microchannels.

Croce et al[4] used a computational approach to model conical roughness elements and their effect on flow through microchannels. Like Kandlikar, he also reports a shift in the friction factor due to surface roughness, and compares the results of his computational analysis to the equations proposed by several authors for the constricted hydraulic diameter for two different roughness element periodicities. While the results of his analysis match Kandlikar's equation ($D_{cf} = D_t - 2\varepsilon$) within 2% for one case, for a higher periodicity Kandlikar's approximation deviates from numerical results by 10%. This example, and others discussed in Croce's paper, begin to outline how roughness properties other than height can effect a shift in the flow Poiseuille number.

Gamrat et al.[10] provides a detailed summary of previous studies reporting Poiseuille number increases with surface roughness. He then develops a semi-empirical model using both experimental data and numerical results to predict the influence of surface roughness on the Poiseuille number. Gamrat's analysis, to the best of the author's knowledge, is the most thorough attempt to predict the effects of surface roughness on the Poiseuille number of laminar flow in microchannels.

There appears to have been no prior efforts to model and quantitatively predict the impact of this type of drag enhancement on turbine performance. The integral perturbation analysis can be modified to incorporate the effects of enhanced drag due to surface microstructuring. The goal of this analysis is to model surface roughness effects on momentum transport in drag-type turbines in the most general way; therefore surface roughness is modeled as an increase in Poiseuille number, as reported by Croce and Gamrat. The development of the integral perturbation analysis and evaluation of its predictions are described in the following sections.

1.4 Organization

Chapter 2 describes the authors' methodology in characterizing and understanding turbines, and outline the experimental studies to which the analysis is compared

Chapter 3 describes the development of the integral perturbation solution to the flow field in the Tesla rotor, and the conclusions made from the resulting equations.

Chapter 4 describes the computational modeling done in ANSYS/Fluent to verify the mili-watt scale water turbine, and the assumptions made in the analytical treatment of flow.

Chapter 5 will discuss the data gathered from a combination of the experimental, analytical, and numerical analyses.

Finally, Chapter 6 will outline the conclusions made by this study.

Chapter 2

Methodology

2.1 Goals of Study

The goal of this study is to develop a more thorough characterization of flow through Tesla turbines, and to use that framework to understand and develop performance enhancement strategies, and finally to outline potential opportunities and markets for devices of this type. To accomplish this goal, an analysis is developed that is more thorough and useful than previous analyses. The validity of this analysis is evaluated by comparison to previously published test data, and to CFD simulations of the flow through Tesla turbines. Finally, conclusions are made based on the comparison of an analytical understanding of turbine operation, test data, and computational results.

2.2 Summary of Integral Perturbation Approach to Evaluating the Flow Through the Rotor

In Chapter 3, the analytical treatment of flow in the rotor begins by considering the flow through the nozzle which is delivered through the rotor. Then, the continuity and momentum equations in cylindrical coordinates are described, along with the simplifying assumptions that are applied to them. Next, a parabolic velocity profile is postulated, as a function of the Poiseuille number. This velocity profile is substituted into the momentum equations, which are then integrated across the microchannel width, and the resulting equations are simplified in terms of several non-dimensional parameters. The terms in this equation are grouped based on the aspect ratio of the channel ($\varepsilon = D_H/r_o = 2b/r_o$), which is typically very small. It is postulated that the higher order groups of terms (those multiplied by ε^1 or ε^2) are small compared to groups multiplied by ε^0, and the resulting differential equations can be solved explicitly. The higher order ($\varepsilon = D_H/r_o = 2b/r_o$) terms are solved numerically, and plotted against the lowest order terms, in order to verify that the solution is dominated by the lowest order terms.

The solution is then compared to test data, and an analysis of Tesla turbines based on the resulting equations follows, including a description of optimal ranges of nondimensional parameters, a discussion of the pressure field, a visualization of streamlines in the rotor, and a discussion of the effect of modifying the friction factor in the channels via microstructured surfaces.

2.3 Air Turbine Experimental Set-up

This work was previously published in [18], and a summary of the experimental set-up is provided here in order to proivde context for the analysis and comparison the experimental resutls that follows in Chapter 3.

The turbine used for this test was purchased from gyroscope.com and was tested with compressed air. In both the inlet and outlet to the turbine, the air hose was connected to a 5 long piece of 2 aluminum hex bar stock. The bar stock was bored through with fittings on each end to attach the air hose to the turbine. The walls of the bar stock provided enough space to drill and tap threaded holes for the thermocouple plug and the pressure tap. Both of these aluminum instrument mounts were secured with a piece of dampening foam to reduce torque on the fittings and to dampen vibrations. Temperature and pressure were measured at three locations; the inlet pipe, inside the turbine just after the nozzle, and in the exhaust pipe. Temperatures were measured using K- type thermocouple probes, and pressures were measured using static pressure taps connected to pressure transducers.

Air flow rate was read manually using a vertical mount variable-area flow-meter. A digital tachometer was used to measure rpm. Turbine shaft work was used to power a three- phase generator and power output was recorded by measuring the voltage over 3 resistors in a delta configuration. The resistances on the generator can be changed to vary the load on the generator and thus the torque on the turbine. A USB data acquisition pad and/or a voltmeter was used to collect the RMS voltage data from the resistors and pressure transducers. A separate data acquisition pad with a built-in amplifier was used to collect data from the three thermocouples. Data was read either with MATLAB or LabVIEW, and data taken with LabVIEW was imported into MATLAB for processing. The entire system configuration can be seen in Figure 2.1.

A dynamometer was later built to characterize the accuracy of the generator power measurement. The turbine generator mount was modified so that the static part of the generator, formerly fixed to the turbine, was mounted on the inner race of a bearing, and the outer race was mounted to the turbine. This allowed the static portion of the generator to spin freely. It was held in place by a lever arm attached to a load cell, with the other end of the load cell fixed on the stationary part of the dynamometer (outer bearing race). The aluminum turbine disks measure 73 mm in diameter and 1.2 mm thick. The disks are assembled on a 6 mm shaft with 1.2 mm spacers. The nozzle is a cylindrical brass chamber with 9 holes drilled through the wall which align with the gaps between the 10 turbine disks. The nozzle angle can be adjusted while the turbine is assembled and operational using a

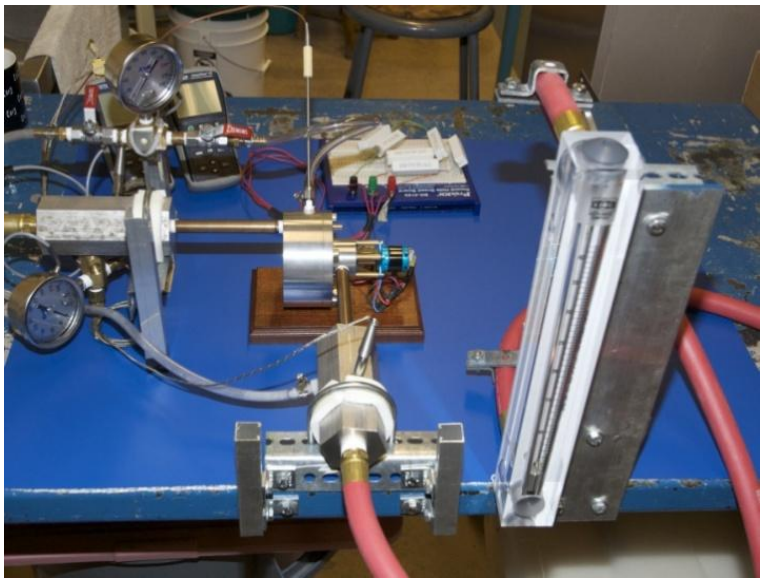

Figure 2.1: Air Turbine Test Setup

screwdriver. The optimal angle for the nozzle was slightly less than tangent to the disk. The optimal angle was found by adjusting the nozzle angle until the highest power was reached. The turbine rotor and nozzle can be seen in Figure 2.2.

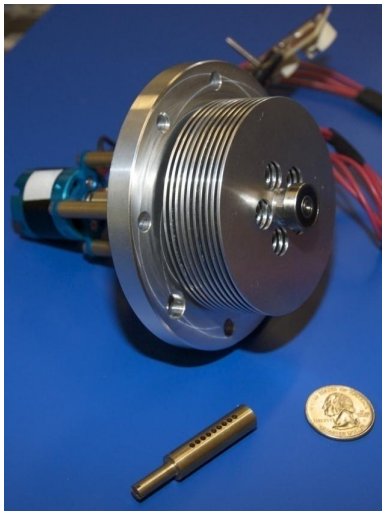

Figure 2.2: Photograph of the Tesla rotor tested with air

A final modification to turbine hardware was performed to test the ability of the model to predict efficiency as a function of turbine geometry. The analysis presented in [2] and [18] concluded that lower Reynolds numbers are desired. Since Reynolds number is proportional

to flow rate and gap size, increasing the number of disks decreases Reynolds number by decreasing the flow per disk and the gap size. New disks were manufactured out of 7075 aluminum sheet at 0.8 mm thick, or 2/3rds of the original disk thickness. New spacers were manufactured from 0.4 mm aluminum shim stock, or 1/3rd the value of the previous washers. This allowed the disk spacing to be reduced by 66% and the number of disks to be increased by 100%, which, all other operating conditions being constant, would result in a 6- fold decrease in the Reynolds number. The new rotor is shown in Figure 2.3.

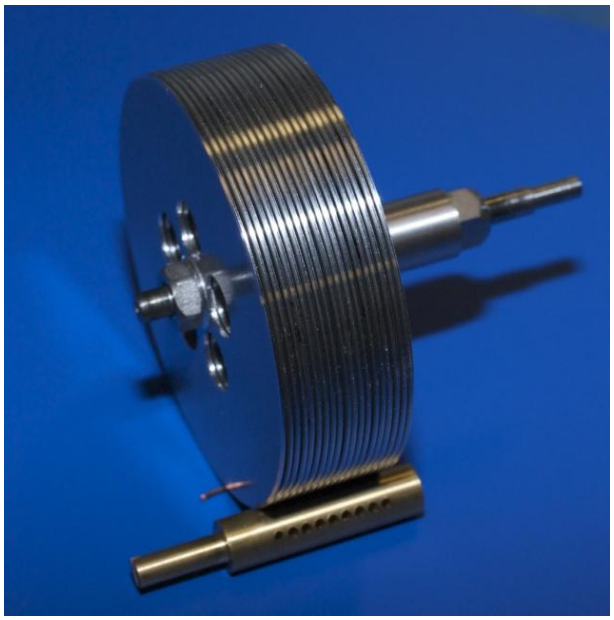

Figure 2.3: Photograph of the redesigned Tesla rotor tested with air

2.4 Water Turbine Experimental Set-up

In this section the fabrication, experimental methods, and data analysis for a mm-scale turbine using water as a working fluid are briefly discussed. More detailed information is presented in [14].

Rotor and Turbine Assembly

Disks of 1 and 2 cm diameters with three different center exhaust hole patterns were fabricated using commercial photo etching (Microphoto, Inc., Roseville, MI) on 125μm thick, 300 series full hard stainless steel sheets (Figure 2.4, Table 2.1). A square axle with rounded ends was used to enable automatic alignment of the disks. The spacers were 125μm thick.

Four different rotor stacks were assembled with 1 cm diameter disks. Two rotors with 125μm inter-disk spacing but with different exhaust hole designs, one rotor with 250μm

Table 2.1: Rotor Specifications. Rotors are photo-etched stainless steel and are assembled manually.

Rotor #	Rotor dia. (cm)	Disks #	Gap (b) (μm)	ξ_i	A_{exh}/A_{dsk}
1	1	20	125	0.47	0.105
2	1	20	125	0.51	0.143
3	1	13	250	0.47	0.105
4	1	8	500	0.47	0.105
5	2	20	125	0.47	0.105

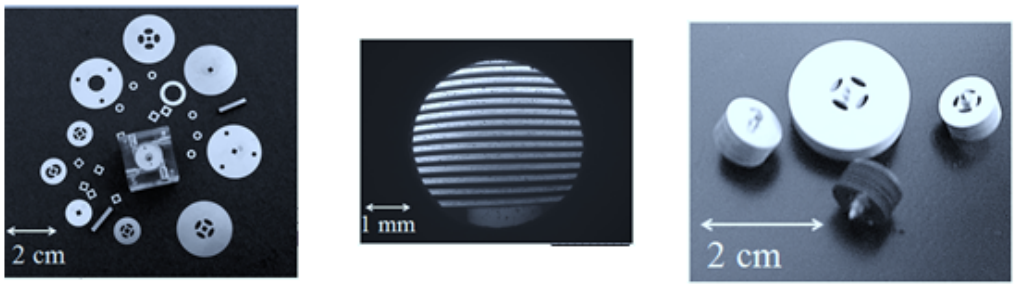

Figure 2.4: Left: components of the rotors - stainless steel disks, bronze square axle, spacers, end disks. Middle: Rotor-1, 20 x white light microscopy showing 125μm disk and gap uniformity. Right: assembled 1cm and 2cm rotors

spacing, and one rotor with 500μm spacing were tested. The number of disks in the rotor assemblies varied (20, 13 and 8, respectively) to fit in the same enclosure. The rotors were held tight by two screws on either side. Ruby Vee bearings (1.25 mm, Bird Precision, Waltham, MA) connected the shaft to the housing. These bearings perform well at speeds less than $10,000$ RPM.

Nozzle Design

To explore the nozzle parameter space, 3D plastic rapid prototyping was used (ProtoTherm 12120 polymer, 0.002 layer thickness, High-Resolution Stereolithography 3, FineLine Prototyping, Inc., Raleigh, NC) to facilitate nozzle designs which would otherwise be unmachinable. Three different shapes, three different areas, and four different angles of entry are used in this design (Figure 2.5, Table 2.2). Nozzles 1-4, 6, and 8 are circular at the nozzle entry (upstream) and are slit, or oblong shaped, at the nozzle exit (downstream, feeding into the turbine). Nozzle 5 also begins circular but then splits into five small nozzles. Nozzle 7 is similar to nozzles 1-4, 6, and 8 but has the largest exit area, i.e. the nozzle area increases, as opposed to decreases, from the entry to the exit. These details, as well as the arcwise span

Table 2.2: Nozzle Specifications. 3D plastic prototype ProtoTherm 12120 polymer 0.002 High resolution Stereo lithography - Fine Line Prototyping Inc.

Nozzle #	Type	Area (mm^2)	angle (deg)	arcwidth (deg)
1	Circular to slit	3.28	15	19
2	Circular to slit	3.28	25	16
3	Circular to slit	2.28	0	37
4,8	Circular to slit	3.28	0	37
5	Circular to 5 circles	0.69	15	19
6	Circular to slit	3.28	35	14
7	Circular to diverging slit	7.14	15	19

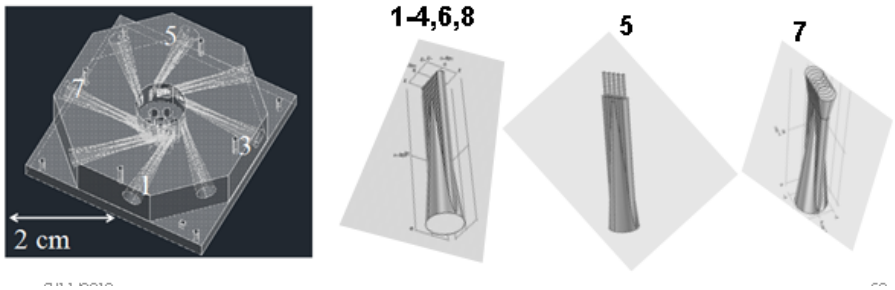

Figure 2.5: left: exploded view of the turbine enclosure with the nozzles, right: 3 types of nozzles

of the nozzle exits, are tabulated in Table 2.2.

Water Test setup

In this application, the turbine shaft would produce electricity via an electrical transduction mechanism, such as capacitive coupling or microscale induction generation, as opposed to driving outer machinery to do mechanical work. For this experiment, shaft torque, power, and efficiency are measured without an external shaft. Figure 2.6 shows the test setup. A gear pump (EW-74014-40, Cole-Parmer Instrument Company, Vernon Hills, IL) was used to produce 1 - 20 mL/sec flow rates while the pressure at the nozzle inlet was measured (DPG8000-100, Omega Engineering, Inc, Stamford, CT). During operation, the rotation of the turbine was recorded using a high speed video camera (FASTCAM-X 1024PCI, Photron, San Diego, CA using PFC Viewer software). Thermocouples at the top and bottom of the enclosure (5SC-TT-K-40-36, Omega Engineering, Inc., Stamford, CT) monitored turbine temperature.

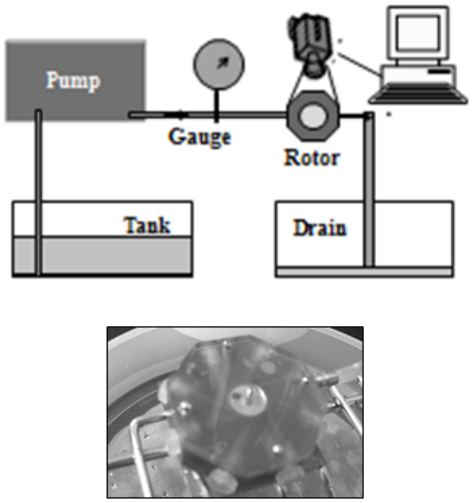

Figure 2.6: Top: gear pump draws water from a tank and drives the rotor. The nozzle inlet pressure is measured using a gauge and the rotor movement is recorded using high speed camera. Bottom: tested turbine rotor housing diameter is 1.013 cm. All nozzle entry hole diameters are 4.04 mm

Data Collection and Processing

Data collection began when the turbine was at rest. Flow was then initiated, and once the rotor speed stabilized, flow was halted, and data collection continued until the turbine was at rest. Angular accelerations and decelerations were computed from video data by performing polynomial curve fits on the frequency vs. time data and extracting the fitted curves' slopes at given frequencies (Figure 2.7). At a specific rotor RPM, the acceleration of the turbine multiplied by the polar moment of inertia of the rotor represents the torque being exerted by the fluid on the rotor, minus any losses, assuming quasi-steady state fluid flow at that time. Similarly, at a specific rotor RPM, the deceleration of the rotor after the fluid flow has been stopped, multiplied by the moment of inertia of the rotor, represents the torque exerted by the loss mechanisms, mainly bearing friction and the viscous forces between the stationary turbine casing and the rotating rotor. The sum of these two torques represents the total torque exerted by the fluid on the rotor, and is the appropriate torque to compare to the analytical and ANSYS predictions of turbine efficiency, which do not have the capability of modeling bearing friction or viscous losses between the rotor and the turbine casing. A similar procedure for torque calculation is used in [12]. The test data analysis is described in equations 2.1 - 2.3, where τ is the torque (N·m), J is the moment of inertia of the rotor (kg·m^2) which was derived from the geometry of the rotor components, α_1 and α_2 are the acceleration and deceleration, $\dot{\mathcal{W}}$ is the shaft power, and f is the rotor rotational frequency.

$$\tau = J(\alpha_1 - \alpha_2) \tag{2.1}$$

$$\dot{\mathcal{W}} = 2\pi f \tau \tag{2.2}$$

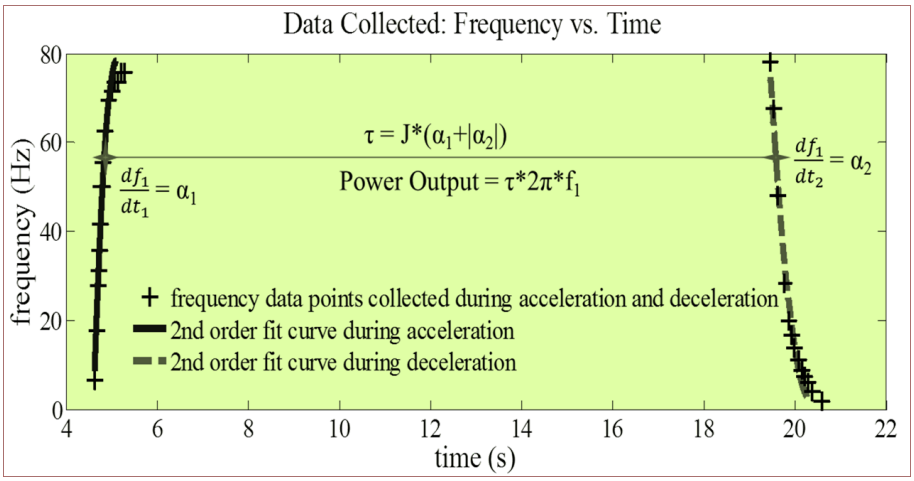

Figure 2.7: Sample raw video data (+), 2nd to 5th order polynomial curve fits for the acceleration and deceleration.

$$\eta_{exp} = \frac{\dot{\mathcal{W}}}{(\dot{m}/\rho)P} \tag{2.3}$$

Experimental Uncertainty: 12%

Turbine design, fabrication, and test set-up were designed for rapid iteration and simplicity, for the sake of identifying problems in mm-scale turbine design and for deriving optimum design parameters. Fabrication, test procedure and test data analysis each contribute to an uncertainty of 4%, 5% and 10% respectively. All are treated as independent random processes for estimating the overall uncertainty of 12%.

Fabrication Uncertainty: 4%

The fabrication uncertainty changes the design point, but stays about the same during the testing. This would affect the comparisons between the predicted and experimental results as the predicted result is based on the design points. The enclosure and the nozzles are fabricated using 3D prototyping with 50μm resolution. The nozzle dimensions are in mm and for a fixed RPM and flow rate, a 1% dimensional uncertainty results in about 2% velocity and 4% shaft power uncertainty. It also results in about 7% nozzle drop uncertainty, though the effect of that on the turbine performance is less than 0.5%. in the tested flow range.

Test procedure Uncertainty: 5%

The rotor is positioned in the enclosure manually and has a positional uncertainty of the order of 100μm. The rotor also showed some warping as tests progressed. As one enclosure is used for testing all the rotors, a 5% uncertainty in shaft power is estimated.

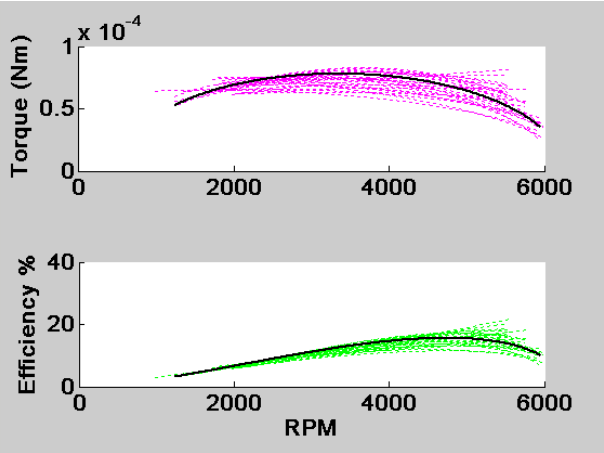

Figure 2.8: Rotor-1 Nozzle-3 Flow rate 600ml/m - The curve fit results of Torque and Efficiency against Frequency and the selected optimum curve

Test data and analysis Uncertainty: 10%

The moment of inertia of the rotor is calculated based on the components in the rotor assembly. It is not verified using simulation. The frame rate of the recording and the markings on the rotor top disk dictate the accuracy in the estimation of the acceleration and deceleration rates. Though the steady state RPM is averaged over many revolutions and is accurate to 1%, the transition areas which are used for the main up and down torque calculations have fewer data points. To get a good prediction, 27 pairs of curve fits are tried between the two transitional regions and the optimum performing curve based on the goodness of fit, power output and the RPM range is chosen as the test result (Figure 2.8). Peak to peak efficiency variation is about 30% and the standard deviation is about 10%. This dominates the experimental uncertainty.

A summary of the experimental data can be found in Table 2.4.

Table 2.3: Summary of experimental resutls for 10 mm water turbine, designed and tested by Krishnan [14]. Test ID #s are the names used to refer to simulation results in this document. Rotor ID # and Nozzle ID # refer to those in Tables 2.1 and 2.2.

Test ID #	Rotor ID #	# of Disks	Nozzle ID #	Nozzle Area (mm^2)	Nozzle Axial Width (mm)	Power Out (mW)	Volume Flow Rate (ml/min)	Pressure Head (mH_2O)	Efficiency (η_{exp}) (%)
R1N3	1	20	3	2.28	2.5	32	600	2.23	14.7
R1N4-1	1	20	4	3.38	3.5	33	720	2.16	13
R1N4-2	1	20	4	3.38	3.5	0.4	180	0.12	10.9
R1N4-3	1	20	4	3.38	3.5	35	720	2.16	13.7
R1N7	1	20	7	7.14	4.0	15	720	1.74	7.3
R3N3	3	13	3	2.28	2.5	23	600	1.98	11.8
R3N4	3	13	4	3.38	3.5	23	720	2.07	9.22

Chapter 3

Development of Integral Perturbation Solution to Flow Through the Tesla Rotor

An analysis will now be outlined that describes first the flow through the nozzle of the turbine, and then the flow through the microchannels of the turbine, while incorporating a treatment of microstructured walls. The resulting equations for velocity and pressure can be used to solve for the efficiency of the turbine. The closed form solution of the fluid mechanics equations allows a parametric exploration of trends in turbine operation.

Treatment of the Nozzle Delivery of Flow to the Rotor

Before considering the flow in the rotor, a method for predicting the flow exiting the nozzle in Figure 1.1 must be considered. For the purposes of this analysis, the tangential fluid velocity (v_θ) at the outer radius of the rotor (r_o) is taken to be uniform around the circumference of the rotor and equal to the nozzle exit velocity determined from one dimensional compressible flow theory.

In expanders of the type considered here, the flow through the nozzle is often choked. This was the case in expander tests conducted by Rice[17], who reported that virtually all the pressure drop in the device is in the nozzle and little pressure drop occurs in the flow through the rotor. The pressure ratio P_o/P_{nt} across the nozzle for choked flow must be at the critical pressure ratio $(P_t/P_{nt})_{crit}$ at the nozzle inlet temperature. For a perfect gas, this is computed as

$$\left(\frac{P_t}{P_{nt}}\right)_{crit} = \left(\frac{2}{\gamma+1}\right)^{\gamma/(\gamma-1)} \tag{3.1}$$

($(P_t/P_{nt})_{crit}$ is about 0.528 for air at 350 K[15]).

If the nozzle exit velocity is the sonic speed at the nozzle throat, it can be computed for a perfect gas as

$$v_{o,c} = a_t = \sqrt{\gamma R T_t} \tag{3.2}$$

Where T_t, the nozzle throat temperature for choked flow, is given by:

$$T_t = T_{nt}(P_t/P_{nt})_{crit}^{(\gamma-1)/\gamma} \tag{3.3}$$

For isentropic flow through the nozzle, the energy equation dictates that the exit velocity would be

$$v_{o,i} = \sqrt{2c_p T_{nt}\left[1 - (P_o/P_{nt})^{(\gamma-1)/\gamma}\right]} \tag{3.4}$$

and the isentropic efficiency of the nozzle is defined as

$$\eta_{noz} = \frac{v_o^2/2}{v_{o,i}^2/2} \tag{3.5}$$

It follows from the above relations that for a perfect gas flowing through nozzles with efficiency η_{noz}, the tangential velocity of gas into the rotor at $r = r_o$, taken to be equal to the nozzle exit velocity, is given by

$$(v_\theta)_{r=r_o} = v_o = \sqrt{\eta_{noz}} v_{o,i} \tag{3.6}$$

Where $v_{o,i}$ is computed using equation (3.4), and for choked flow the nozzle efficiency is given by

$$\eta_{noz} = \frac{\gamma R (P_t/P_{nt})_{crit}^{(\gamma-1)/\gamma}}{2c_p\left[1 - (P_o/P_{nt})^{(\gamma-1)/\gamma}\right]} \tag{3.7}$$

Treating the gas flow as an ideal gas with nominally constant specific heat, equation (3.6) provides the means of determining the rotor gas inlet tangential velocity $(v_\theta)_{r=r_o}$ given the specified flow conditions for the nozzle.

Analysis of the Momentum Transport in the Rotor

For steady incompressible laminar flow in microchannels between the turbine rotor disks, the governing equations for the flow are:

Continuity:

$$\nabla \cdot \mathbf{v} = 0 \tag{3.8}$$

Momentum:

$$\mathbf{v} \cdot \nabla \mathbf{v} = -\frac{\nabla P}{\rho} + \nu \nabla^2 \mathbf{v} + \mathbf{f} \tag{3.9}$$

Treatment of the flow as incompressible is justified by the observation of Rice[17] that minimal pressure drop occurs in the rotor under typical operating conditions for this type of expander. For this analysis, the following idealizations are adopted:

1. The flow is taken to be steady, laminar, and two-dimensional: $v_z = 0$ and the z-direction momentum equation has a trivial solution.
2. The flow field is taken to be radially symmetric. The inlet flow at the rotor outer edge is uniform, resulting in a flow field that is the same at any angle θ. All θ derivatives of flow quantities are therefore zero.
3. Body force effects are taken to be zero.
4. Entrance and exit effects are not considered. Only flow between adjacent rotating disks is modeled.

With the idealizations noted above, the governing equations (3.8) and (3.9), in cylindrical coordinates, reduce to:

Continuity:

$$\frac{1}{r}\frac{\partial(rv_r)}{\partial r} = 0 \tag{3.10}$$

r-direction momentum:

$$\begin{aligned} v_r\frac{\partial v_r}{\partial r} - \frac{v_\theta^2}{r} = & - \frac{1}{\rho}\left(\frac{\partial P}{\partial r}\right) \\ & + \nu\left\{\frac{1}{r}\frac{\partial}{\partial r}\left(r\frac{\partial v_r}{\partial r}\right) + \frac{\partial^2 v_r}{\partial z^2} - \frac{v_r}{r^2}\right\} \end{aligned} \tag{3.11}$$

θ-direction momentum:

$$v_r\frac{\partial v_\theta}{\partial r} + \frac{v_r v_\theta}{r} = \nu\left\{\frac{1}{r}\frac{\partial}{\partial r}\left(r\frac{\partial v_\theta}{\partial r}\right) + \frac{\partial^2 v_\theta}{\partial z^2} - \frac{v_\theta}{r^2}\right\} \tag{3.12}$$

z-direction momentum:

$$0 = -\frac{1}{\rho}\left(\frac{\partial P}{\partial z}\right) \tag{3.13}$$

Equation (3.13) dictates that the pressure is uniform across the channel at any (r, θ) location. For the variations of the radial and tangential velocities, the following solution forms are postulated:

$$v_r = \bar{v}_r(r)\phi(z) \tag{3.14}$$
$$v_\theta = \hat{v}_\theta(r)\phi(z) + U(r) \tag{3.15}$$

where

$$\phi(z) = \left(\frac{n+1}{n}\right)\left[1 - \left(\frac{2z}{b}\right)^n\right] \tag{3.16}$$

and $\bar{v}_r$ and $\hat{v}_\theta$ are mean velocities defined as

$$\bar{v}_r(r) = \frac{1}{b}\int_{-b/2}^{b/2} v_r dz \tag{3.17}$$
$$\hat{v}_\theta(r) = \frac{1}{b}\int_{-b/2}^{b/2} (v_\theta - U) dz \tag{3.18}$$

Where b is the gap distance between disks.

For laminar flow in the tangential direction, the wall shear is related to the difference between the mean local gas tangential velocity and the rotor surface tangential velocity ($\hat{v}_\theta = \bar{v}_\theta - U$) through the friction factor definition

$$\tau_w = f\frac{\rho\hat{v}_\theta^2}{2} \tag{3.19}$$

For a Newtonian fluid, it follows that

$$f = \frac{\tau}{\rho\hat{v}_\theta^2/2} = \frac{\mu[\partial(v_\theta - U)/\partial z]_{z=b/z}}{\rho\hat{v}_\theta^2} \tag{3.20}$$

For the purposes of this analysis, the tangential shear interaction of the flow with the disk surface is postulated to be equivalent to that for laminar Poiseuille flow between parallel plates

$$f = \frac{\mathrm{Po}}{\mathrm{Re}_c} \tag{3.21}$$

Where here Re_c is the Reynolds number defined as

$$\mathrm{Re}_c = \frac{\rho\hat{v}_\theta D_H}{\mu} \tag{3.22}$$
$$D_H = 2b \tag{3.23}$$

and Po is a numerical constant usually referred to as the Poiseuille number. For flow between smooth flat plates, the well-known laminar flow solution predicts Po = 24. For

flow between flat plates with roughened surfaces, experiments[13][4][10] indicate that a value other than 24 better matches pressure loss data. We therefore define an enhancement number F_{Po} as

$$F_{\mathrm{Po}} = \mathrm{Po}/24 \tag{3.24}$$

which quantifies the enhancement of shear drag that may result from disk surface geometry modifications. Note that Eqs. (3.19) - (3.23) dictate that for the postulated v_θ form (3.15)

$$(n+1) = \mathrm{Po}/8 = 3F_{\mathrm{Po}} \tag{3.25}$$

It follows that:

- for laminar flow over smooth walls: $n = 2$, $\mathrm{Po} = 24$, $F_{\mathrm{Po}} = 1$
- for laminar flow over walls with drag enhancing roughness: $n > 2$, $\mathrm{Po} > 24$, $F_{\mathrm{Po}} > 1$

The variation of the velocity profile with n is shown in Fig. 3.1.

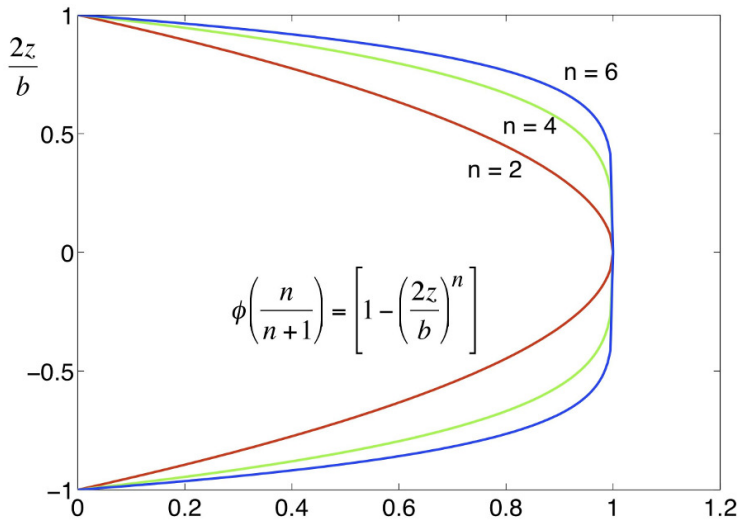

Figure 3.1: Variation of Velocity Profile with n

Radial Velocity Solution from the Continuity Equation

Substituting (3.14) into (3.10) and integrating with respect to r yields

$$rv_r = r\bar{v}_r\phi = constant = C_r \tag{3.26}$$

Integrating equation 3.10 across the channel and using the fact that

$$\int_{-b/2}^{b/2} \phi dz = 2\int_{0}^{b/2} \phi dz = b \tag{3.27}$$

yields

$$\int_{-b/2}^{b/2} rv_r dz = \int_{-b/2}^{b/2} r\bar{v}_r\phi dz = r\bar{v}_r b = bC_r = C_r' \tag{3.28}$$

Mass conservation requires that

$$\begin{aligned} -2\pi r_o\rho\int_{-b/2}^{b/2} v_r dz &= -2\pi r_o\rho\bar{v}_r(r_o)\int_{-b/2}^{b/2}\phi dz \\ &= -2\pi r_o\rho\bar{v}_r(r_o)b = \dot{m}_c \end{aligned} \tag{3.29}$$

Where $\dot{m}_c$ is the mass flow rate per channel between rotors. Combining (3.28) and (3.29) yields the following solution for the radial velocity

$$\bar{v}_r = -\frac{r_o\bar{v}_{ro}}{r} \tag{3.30}$$

Where

$$\bar{v}_{ro} = \frac{\dot{m}_c}{2\pi r_o\rho b} \tag{3.31}$$

Solution of the Tangential and Radial Momentum Equations

The next step is to substitute the postulated solutions from (3.14) and (3.15) into the tangential and radial momentum equations (3.12) and (3.11), integrate each term across the microchannel, and use (3.27) together with the results

$$\int_{-b/2}^{b/2} \phi^2 dz = 2\int_{0}^{b/2} \phi^2 dz = \frac{2(n+1)}{2n+1}b \tag{3.32}$$

$$\begin{aligned} \int_{-b/2}^{b/2}\left(\frac{d^2\phi}{dz^2}\right)dz &= 2\int_{0}^{b/2}\left(\frac{d^2\phi}{dz^2}\right)dz \\ &= -\frac{4(n+1)}{b} \end{aligned} \tag{3.33}$$

doing so and introducing the dimensionless variables:

$$\xi = r/r_o \tag{3.34}$$
$$\hat{W} = \hat{v}_\theta/U_o = (\bar{v}_\theta - U)/U_o \tag{3.35}$$
$$\hat{P} = (P - P_o)/(\rho U_o^2/2) \tag{3.36}$$
$$V_{ro} = \bar{v}_{ro}/U_o \tag{3.37}$$
$$\varepsilon = 2b/r_o \tag{3.38}$$
$$\mathrm{Re}_m^* = (D_H/r_o)\frac{\dot{m}_c D_H}{2\pi r_o b\mu} = \frac{D_H \dot{m}_c}{\pi r_o^2 \mu} \tag{3.39}$$

converts equations (3.11) and (3.12) to the forms

$$\frac{\partial \hat{P}}{\partial \xi} = \hat{P}' = \frac{4(n+1)}{(2n+1)\xi^3}\left(V_{ro}^2 + \hat{W}^2\xi^2\right) + 4\hat{W} + 2\xi + 32(n+1)\frac{V_{ro}^2}{\mathrm{Re}_m^*\xi} \tag{3.40}$$

$$-\frac{2n+1}{n+1} = \left(\frac{2n+1}{2(n+1)}\frac{\varepsilon^2}{\mathrm{Re}_m^*}\right)\xi\hat{W}'' + \left(\frac{2n+1}{2(n+1)}\frac{\varepsilon^2}{\mathrm{Re}_m^*} + 1\right)\hat{W}' + \left(\left[1 - \frac{2n+1}{2(n+1)}\frac{\varepsilon^2}{\mathrm{Re}_m^*}\right]\frac{1}{\xi} - \frac{8(2n+1)\xi}{\mathrm{Re}_m^*}\right)\hat{W} \tag{3.41}$$

Where $\hat{W}' = d\hat{W}/d\xi$ and $\hat{W}'' = d^2\hat{W}/d\xi^2$. Solution of these equations requires boundary conditions on the dimensionless relative velocity and the dimensionless pressure ($\hat{W}$ and $\hat{P}$). Here it is assumed that the gas tangential velocity and the disk rotational speed are specified, so $\hat{W}$ at the outer radius of the disk is specified. It follows that

$$\text{at } \xi = 1;\ \hat{W}(1) = \hat{W}_o \tag{3.42}$$

In addition, from the definition of $\hat{P}$, it follows that

$$\hat{P}(1) = 0 \tag{3.43}$$

Equations (3.42) - (3.43) provide boundary conditions for solution of the dimensionless tangential momentum equation (3.41) and the radial momentum equation (3.40), which predicts the radial pressure distribution.

Since $\varepsilon = 2b/r_o$ is much less than 1 in the systems of interest here, we postulate a series expansion solution of the form

$$\hat{W} = \hat{W}_0 + \varepsilon\hat{W}_1 + \varepsilon^2\hat{W}_2 + \dots \tag{3.44}$$

$$\hat{P} = \hat{P}_0 + \varepsilon\hat{P}_1 + \varepsilon^2\hat{P}_2 + \dots \tag{3.45}$$

Substituting results in equations (3.46) - (3.54).
O(ε^0):

$$\begin{aligned} -\frac{6F_{\mathrm{Po}}-1}{3F_{\mathrm{Po}}} &= \hat{W}_0' \\ +\left(\frac{1}{\xi} - 8(6F_{\mathrm{Po}}-1)\frac{\xi}{\mathrm{Re}_m^*}\right)\hat{W}_0 & \end{aligned} \tag{3.46}$$

$$\begin{aligned} \hat{P}_0' = \frac{12F_{\mathrm{Po}}}{6F_{\mathrm{Po}}-1}\frac{1}{\xi^3}\left(V_{ro}^2 + \hat{W}_0^2\xi^2\right) \\ +4\hat{W}_0 + 2\xi + V_{ro}^2 F_{\mathrm{Po}}\frac{96}{\mathrm{Re}_m^*\xi} \end{aligned} \tag{3.47}$$

$$\text{at } \xi = 1: \ \hat{W}_0 = \hat{W}_{0,r_o}, \ \hat{P}_0 = 0 \tag{3.48}$$

O(ε^1):

$$0 = \hat{W}_1' + \left(\frac{1}{\xi} - 8(6F_{\mathrm{Po}}-1)\frac{\xi}{\mathrm{Re}_m^*}\right)\hat{W}_1 \tag{3.49}$$

$$\hat{P}_1' = \frac{12F_{\mathrm{Po}}}{6F_{\mathrm{Po}}-1}\frac{1}{\xi}2\hat{W}_0\hat{W}_1 + 4\hat{W}_1 \tag{3.50}$$

$$\text{at } \xi = 1: \ \hat{W}_1 = 0, \ \hat{P}_1 = 0 \tag{3.51}$$

O(ε^2):

$$\begin{aligned} -\hat{W}_2' - \left(\frac{1}{\xi} - \frac{8(2n+1)\xi}{\mathrm{Re}_m^*}\right)\hat{W}_2 \\ = \frac{6F_{\mathrm{Po}}-1}{6F_{\mathrm{Po}}}\left(\frac{\xi\hat{W}_0''}{\mathrm{Re}_m^*} + \frac{\hat{W}_0'}{\mathrm{Re}_m^*} - \frac{\hat{W}_0}{\mathrm{Re}_m^*\xi}\right) \end{aligned} \tag{3.52}$$

$$\hat{P}_2' = \frac{12F_{\mathrm{Po}}}{6F_{\mathrm{Po}}-1}\frac{1}{\xi}2\hat{W}_0\hat{W}_2 + 4\hat{W}_2 \tag{3.53}$$

$$\text{at } \xi = 1: \ \hat{W}_2 = 0, \ \hat{P}_2 = 0 \tag{3.54}$$

In solving equations (3.46) - (3.54), the dimensionless parameters in the equations

$$\xi_i = r_i/r_o \tag{3.55}$$

$$(\hat{W}_0)_{r_o} = \hat{W}_{0.r_o} = \frac{\bar{v}_{\theta,r_o} - U_o}{U_o} \tag{3.56}$$

$$\mathrm{Re}_m^* = \frac{D_H \dot{m}_c}{\pi r_o^2 \mu} \tag{3.57}$$

$$V_{ro} = \bar{v}_{ro}/U_o \tag{3.58}$$

$$\varepsilon = 2b/r_o \tag{3.59}$$

are dictated by the choices for the following physical parameters:

- r_i, r_o: the inner and outer radii of the disks
- b: the gap between the disks, from which we can compute $D_H = 2b$
- $\dot{m}_c$: the mass flow rate per channel between rotors
- $\omega = U_o/r_o$: the angular rotation rate
- $\bar{v}_{\theta,r_o}$: the mean tangential velocity at the inlet edge of the rotor
- P_o/P_{nt}: pressure ratio
- T_{nt}: nozzle upstream total temperature

Also, for choked nozzle flow, the tangential velocity at the rotor inlet will equal the sonic velocity ($v_{\theta,r_o} = a$). The definitions of M_o and $\hat{W}$ require that the choices for M_o and $\hat{W}_{0,r_o}$ satisfy

$$M_o \equiv U_o/\sqrt{\gamma R T_t} = \frac{(P_t/P_{nt})_{crit}^{(\gamma-1)/2\gamma}}{\hat{W}_{0,r_o} + 1} \tag{3.60}$$

Solving equations (3.46), (3.49) and (3.52) with boundary conditions (3.48), (3.51), and (3.54) gives the following solutions:

$$\hat{W}_0 = \left(\hat{W}_{0,r_o} - \frac{\mathrm{Re}_m^*}{24F_{Po}}\right)\frac{e^{f(\xi)}}{\xi e^{f(1)}} + \frac{\mathrm{Re}_m^*}{24\xi F_{Po}} \tag{3.61}$$

$$\hat{W}_1 = 0 \tag{3.62}$$

$$\hat{W}_2 = \frac{e^{f(\xi)}}{\xi}\int_1^{\xi} \xi^* e^{-f(\xi^*)} g(\xi^*) d\xi^* \tag{3.63}$$

Where

$$g(\xi) = \frac{6F_{\mathrm{Po}} - 1}{6F_{\mathrm{Po}}} \frac{\hat{W}_0/\xi - \hat{W}_0' - \xi\hat{W}_0''}{\mathrm{Re}_m^*} \tag{3.64}$$

$$f(\xi) = \frac{4(6F_{\mathrm{Po}} - 1)\xi^2}{\mathrm{Re}_m^*} \tag{3.65}$$

And ξ^* is a dummy variable of integration.

With this result, the energy efficiency of the rotor and of the turbine, respectively, can be computed using

$$\eta_{rm} = \frac{v_{\theta,o}U_o - v_{\theta,i}U_i}{v_{\theta,o}U_o} \tag{3.66}$$

$$\eta_i = \frac{v_{\theta,o}U_o - v_{\theta,i}U_i}{\Delta h_{isen}} \tag{3.67}$$

Which rearrange to:

$$\eta_{rm} = 1 - \frac{(\hat{W}_i + \xi_i)\xi_i}{\hat{W}_o + 1} \tag{3.68}$$

$$\hat{W}_i = \hat{W}_{\xi=\xi_i=r_i/r_o} \tag{3.69}$$

$$\eta_i = \frac{\left[(\hat{W}_o + 1) - (\hat{W}_i + \xi_i)\xi_i\right](\gamma - 1)M_o^2}{\left[1 - \left(\frac{P_i}{P_{nt}}\right)^{(\gamma-1)/\gamma}\right]} \tag{3.70}$$

The baseline case for comparison with rough wall solutions is that for a smooth wall, or $F_{\mathrm{Po}} = 1$. The solution for $\hat{W}_0$ (equation (3.61)) reduces to:

$$\hat{W}_0 = \left(\hat{W}_{0,r_o} - \frac{\mathrm{Re}_m^*}{24}\right) \frac{e^{\frac{20}{\mathrm{Re}_m^*}(\xi^2-1)}}{\xi} + \frac{\mathrm{Re}_m^*}{24\xi} \tag{3.71}$$

The pressure distribution can be found numerically or analytically by integrating equations (3.47), (3.50), and (3.53).

Higher Order (ε^1, ε^2) Terms

In order to evaluate the significance of the higher order solutions of $\hat{W}$ and $\hat{P}$, equations 3.63 and 3.53 are solved numerically in MATLAB. $\hat{W}_1$ is zero (equation 3.62), and thus $\hat{P}_1$ is also zero by equation 3.50. $\hat{W}_2$ and $\hat{P}_2$ are solved numerically by discretizing the nondimensional

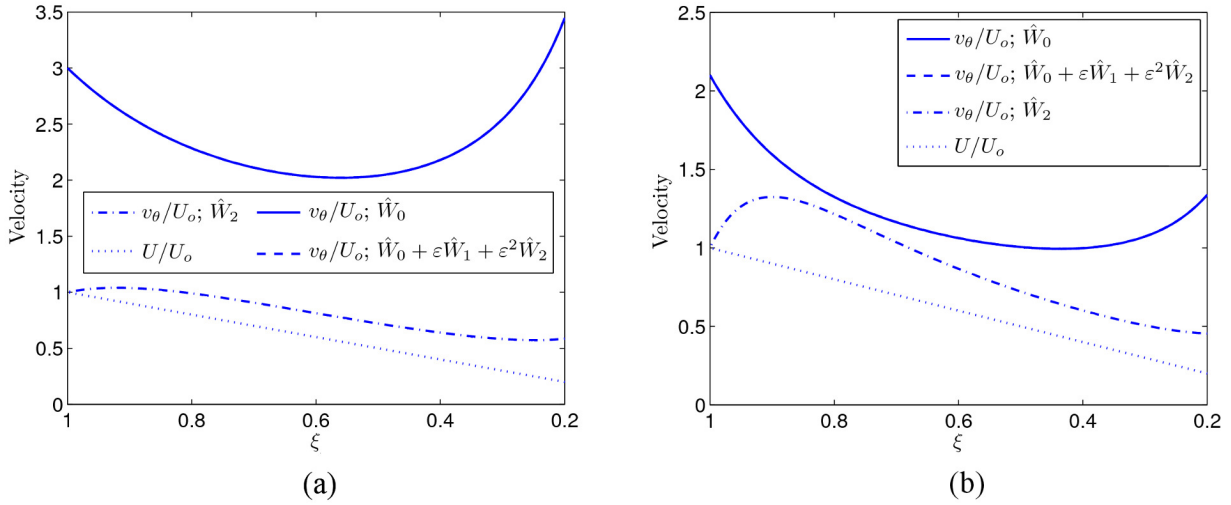

Figure 3.2: Comparison of Velocity plots for 0th order and 2nd order velocity solutions. In both (a) and (b), the plots for $\hat{W}_0$ (solid line) and for $\hat{W}_0 + \varepsilon\hat{W}_1 + \varepsilon^2\hat{W}_2$ (dashed line) are nearly coincident. The dot-dash line ($\hat{W}_2$) is shown to be the same order of magnitude as $\hat{W}_0$, thus making it negligible when multiplied by ε^2. (a) Case 1; $\hat{W}_0 = 2$, $\mathrm{Re}_m^* = 10$, $\xi_i = 0.2$, $V_{ro} = 0.05$, $\varepsilon = 1/20$; choked flow (b) Case 2; $\hat{W}_0 = 1.1$, $\mathrm{Re}_m^* = 5$, $\xi_i = 0.2$, $V_{ro} = 0.05$, $\varepsilon = 1/20$; choked flow

radial coordinate ξ, and carrying out the appropriate integrations and differentiations in equations 3.63 and 3.53. Differentiations are carried out using the forward difference method and integrations are carried out using the trapezoidal method. The discritization of ξ was refined until the solution was unchanged by further refinement.

results are plotted for two different operating conditions in Figures 3.2 (velocity) and 3.3 (pressure). Under both scenarios, the 2nd order terms ($\hat{W}_2$ and $\hat{P}_2$) are shown to be the same order of magnitude as the 0th order terms ($\hat{W}_0$ and $\hat{P}_0$). Velocity plots for $\hat{W}_0$ and for $\hat{W}_0 + \varepsilon\hat{W}_1 + \varepsilon^2\hat{W}_2$ fall nearly directly on top of each other (similarly for $\hat{P}$). For values of ε as high as 1/10, much larger than are found in most systems of interest, both $\varepsilon^2\hat{W}_2$ and $\varepsilon^2\hat{P}_2$ are less than 0.1% of the value of the 0th order term for the two cases shown. Note that equation (3.62) along with equations (3.50) and (3.51) show that $\hat{W}_1 = \hat{P}_1 = 0$. order terms are of the same magnitude as 0th order terms, and knowing that $\varepsilon \ll 1$, equation (3.44) and (3.45) shows that all 2nd order terms can be neglected. Henceforth, we can neglect the 1st and 2nd order terms, and only the 0th order terms ($\hat{W}_0$ and $\hat{P}_0$) will be considered.

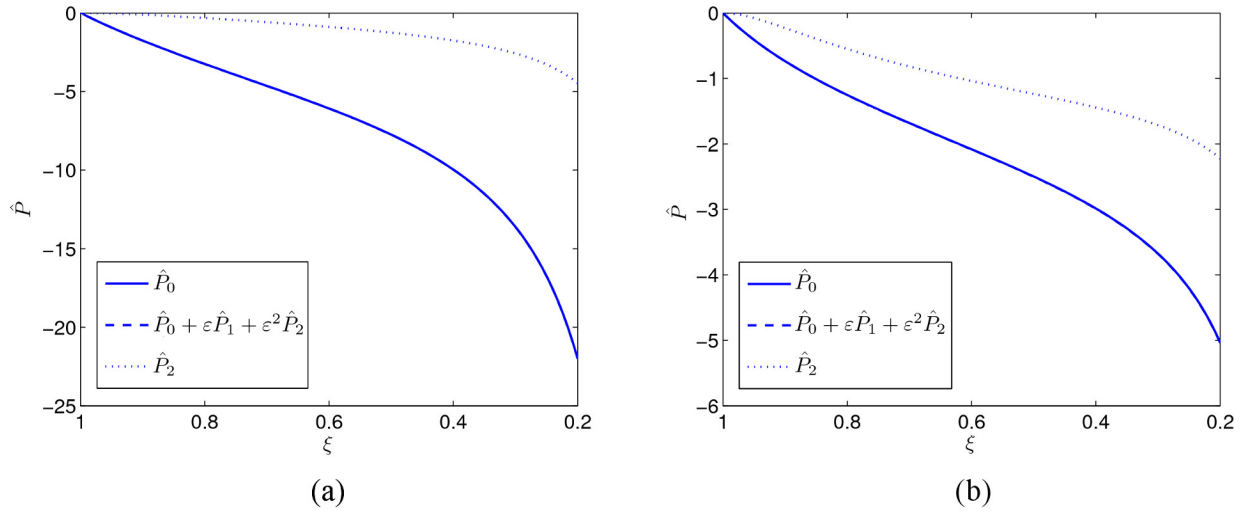

Figure 3.3: Comparison of Pressure plots for 0th order and 2nd order velocity solutions. In both (a) and (b), the plots for $\hat{P}_0$ (solid line) and for $\hat{P}_0+\varepsilon\hat{P}_1+\varepsilon^2\hat{P}_2$ (dashed line) are nearly coincident. The dot-dash line ($\hat{W}_2$) is shown to be the same order of magnitude as $\hat{W}_0$, thus making it negligible when multiplied by ε^2. (a) Case 1; $\hat{W}_0 = 2$, $\mathrm{Re}_m^* = 10$, $\xi_i = 0.2$, $V_{ro} = 0.05$, $\varepsilon = 1/20$; choked flow (b) Case 2; $\hat{W}_0 = 1.1$, $\mathrm{Re}_m^* = 5$, $\xi_i = 0.2$, $V_{ro} = 0.05$, $\varepsilon = 1/20$; choked flow

3.1 Comparison of Smooth Wall Case with Earlier Flow Predictions

The $\hat{W}_0$ solution corresponds closely with the solution developed by Carey[2], only differing by numerical constants. A comparison of results with the model from Carey's earlier model is shown in Figure 3.4. Carey[2] made several assumptions, including ignoring radial pressure effects, treating the flow as inviscid with a body force representation of drag, and ignoring z-derivatives of velocity. In the present analysis, initial assumptions were more conservative and terms were removed based on the arguments of the perturbation analysis. The similarities in the results of this analysis with that of Carey verify that the assumptions made were valid. Additionally, Carey's analysis was compared extensively with experimental data in Romanin[18], so a close correlation between the two approaches is encouraging.

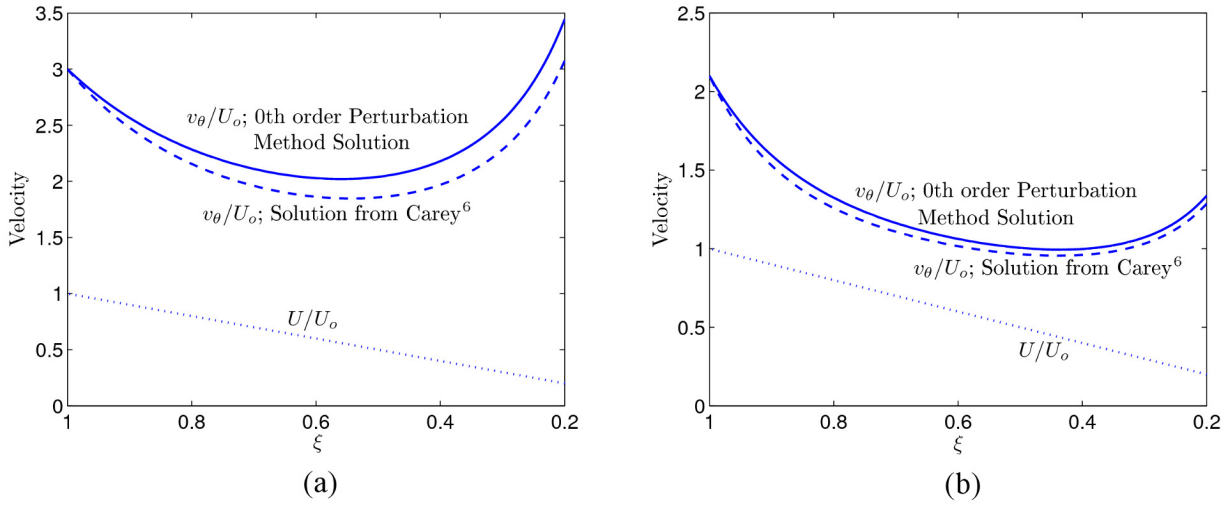

Figure 3.4: Comparison of solutions from the perturbation method and the model developed by Carey[2]. (a) Case 1: $\hat{W}_0 = 2$, $\mathrm{Re}^*_m = 10$, $\xi_i = 0.2$, $V_{ro} = 0.05$, choked flow. The analysis predicts a turbine isentropic efficiency of $\eta_i = 26.1\%$ while the analysis by Carey[2] predicts $\eta_i = 27.0\%$ (b) Case 2: $\hat{W}_0 = 1.1$, $\mathrm{Re}^*_m = 5$, $\xi_i = 0.2$, $V_{ro} = 0.05$, choked flow. The analysis predicts a turbine isentropic efficiency of $\eta_i = 42.3\%$ while the analysis by Carey[2] predicts $\eta_i = 42.5\%$

3.2 Modeling of Flow Velocity with Roughened or Microstructured Surfaces ($F_{\mathrm{Po}} > 1$)

Now that the perturbation analysis has resulted in equations that define the operating conditions and efficiency of the turbine as a function of F_{Po}, we can analyze the effect of surface roughness on turbine performance. Developing a direct correlation between surface roughness and F_{Po} is a detailed process that involves characterizing specific geometric properties of the roughness features and is beyond the scope of this analysis. Here we will only discuss the effects of increasing F_{Po}. Kandlikar[4] reported values for F_{Po} as high as 3.5 for roughened surfaces in microchannels, so values up to $F_{\mathrm{Po}} = 3.5$ will be considered.

Discussion of the Velocity and Pressure Fields

Figure 3.5 shows that the velocity profile is significantly altered by using a roughened surface. Equation (3.70) shows that the exit velocity $\hat{W}_i$ should be minimized to increase efficiency, and indeed the efficiency does increase with F_{Po}. $F_{Po} = 2$ results in a turbine isentropic efficiency of $\eta_i = 45.1\%$, compared to an efficiency of $\eta_i = 42.3\%$ for $F_{Po} = 1$.

Figure 3.6 shows the dimensionless pressure $\hat{P}$ as a function of ξ for several values of F_{Po}.

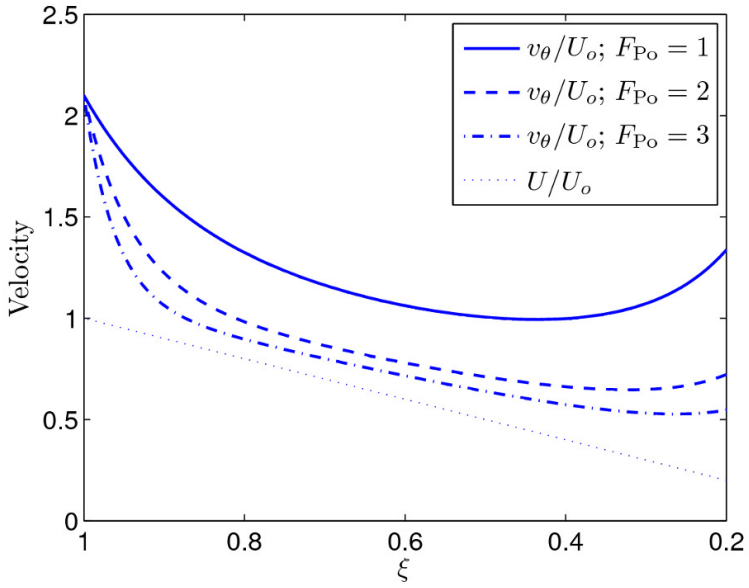

Figure 3.5: Velocity vs. ξ for several values of F_{Po}. $\hat{W}_0 = 1.1$, $\mathrm{Re}_m^* = 5$, $\xi_i = 0.2$; choked flow.

The figure shows that the dimensionless pressure decreases with increasing F_{Po}. This can be attributed to the competing effects of centripetal force and radial pressure. Increasing surface roughness decreases the velocity, and therefore the centripetal force is decreased. The required pressure field to balance the centripetal force on the fluid is therefore also decreased. It is important to note that this does not contradict the conventional knowledge that the pressure drop increases along the direction of the flow as the surface roughness is increased. The pressure drop described here is in the radial direction, while the fluid flow has both a radial and circumferential component.

Performance Enhancement due to Mictrostructured Surfaces

Over the entire range of values for F_{Po} discussed by Croce[4], Figure 3.7 shows that efficiency increases a total of 3.8 percentage points, which amounts to a 9.2% improvement in performance over a smooth wall.

Figure 3.8 shows a surface plot of efficiency as a function of two non-dimensional parameters, Re_M^* and $\hat{W}_{0,r_o}$. It is shown that increasing surface roughness can yield especially significant performance improvements for higher Reynolds numbers rather than lower. Similar trends to those reported by Carey[2] and Romanin[18] can be seen in Figure 3.8; it is clear that high efficiency turbine designs should strive for Reynolds numbers and dimensionless inlet tangential velocity differences to be as small as possible. It is also shown that penalties

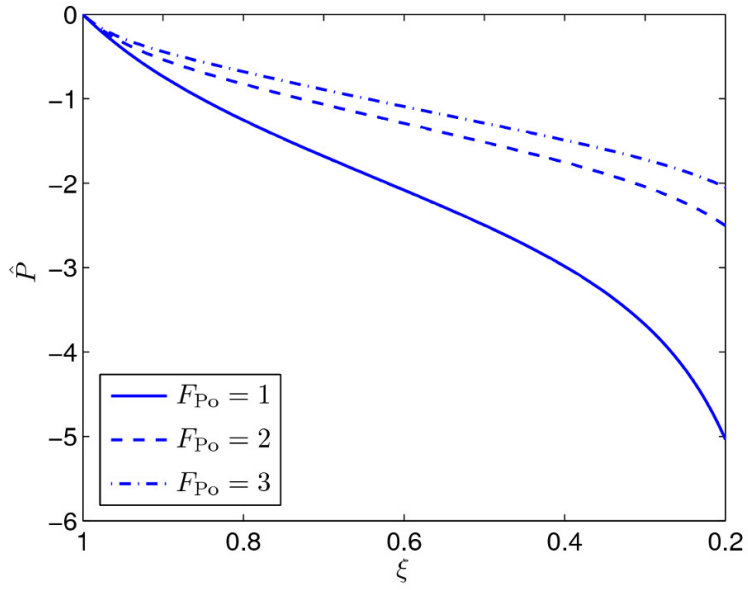

Figure 3.6: Dimensionless Pressure ($\hat{P}$) vs. ξ for several values of F_{Po}. $\hat{W}_0 = 1.1$, $\mathrm{Re}_m^* = 5$, $\xi_i = 0.2$, $V_{ro} = 0.05$; choked flow

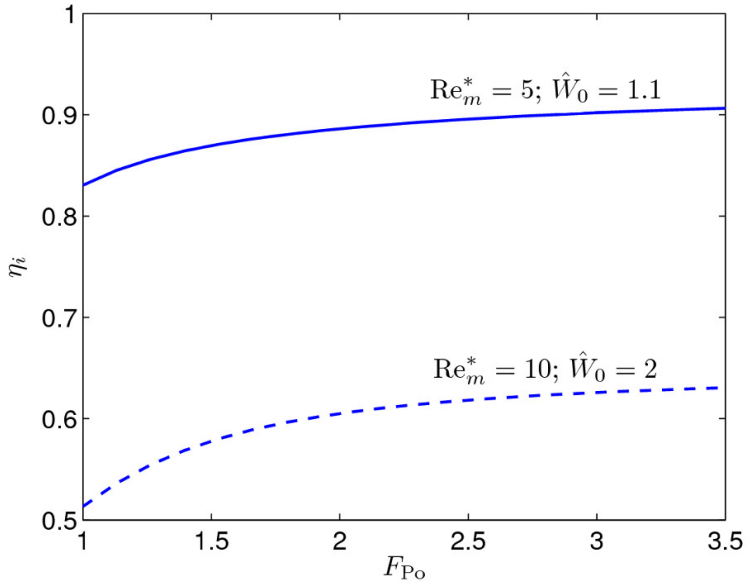

Figure 3.7: Efficiency (η_i) vs. F_{Po} for $\xi_i = 0.2$ and choked flow.

due to higher values of Re_M^* and $\hat{W}_{0,r_o}$ are less dramatic for roughened surfaces.

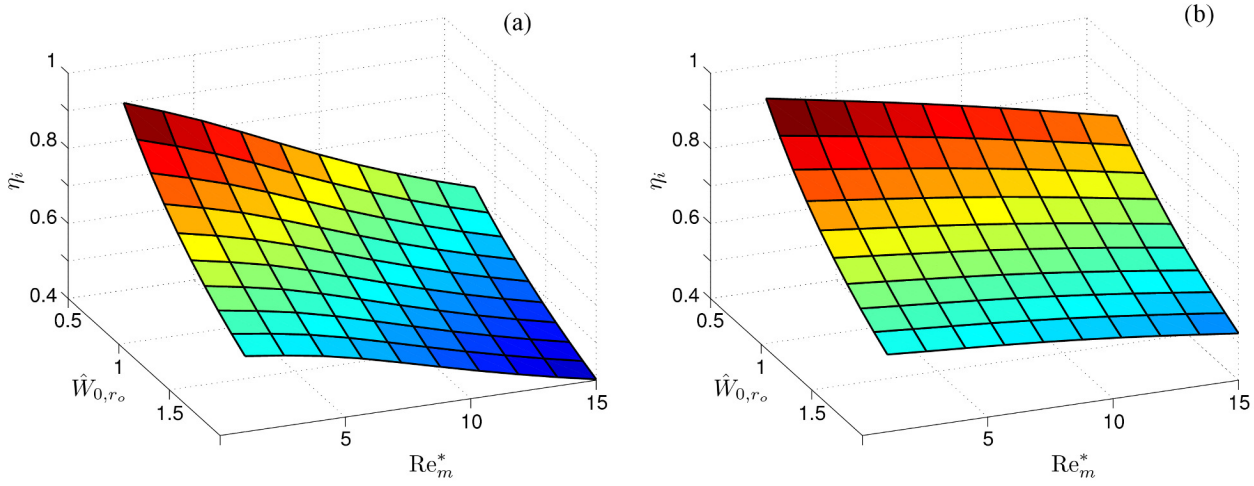

Figure 3.8: A 3D surface plot of efficiency (η_i) as a function of the inlet dimensionless tangential velocity difference ($\hat{W}_{0,r_o}$) and Reynolds number (Re_m^*) for typical operating parameters ($\gamma = 1.4$ (air), $\xi_i = 0.2$, $P_i/P_{nt} = 0.5$, choked flow). (a) $F_{\mathrm{Po}} = 1$ (b) $F_{\mathrm{Po}} = 2$

By taking advantage of microstructured surfaces, larger disk gaps and smaller disks can be used while limiting penalties to efficiency. For example, the nondimensional turbine parameters outlined in case 2 (see Figure 3.2(b)) can be used to deduce the physical parameters in the right hand side of equations (3.55) - (3.59). Using this set of physical parameters, the Poiseuille number can be doubled ($F_{\mathrm{Po}} = 2$), and the radius can be decreased while keeping other parameters constant until the efficiency is equivalent to that achieved by the parameters from case 2 (Figure 3.2(b)). This process results in a turbine radius of $r_o = 18.6$cm, down from $r_o = 34.7$cm in the smooth wall case. In other words, doubling the Poiseuille number, in this case, allowed for a 46% reduction in turbine size with equivalent performance. Similar trade-offs with other physical parameters can be explored, allowing greater flexibility in high-efficiency turbine design. The values outlined in this example are not universal, however, as Figure 3.9 shows that performance increases due to roughened surfaces vary with non-dimensional parameters (e.g. performance increases are less significant at low modified Reynolds (Re_m^*) numbers).

3.3 Streamline Visualization

The model theory developed here also provides the means to determine the trajectory of streamlines in the rotor using the θ and r direction velocity components. Starting at any θ

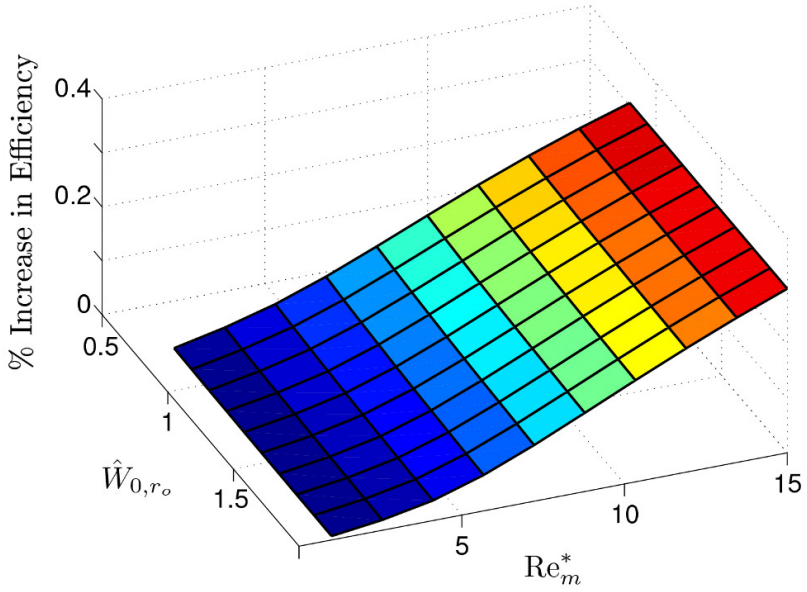

Figure 3.9: A 3D surface plot of the percent increase in efficiency resulting from increasing F_{Po} from 1 to 2 ($(\eta_{i,F_{\mathrm{Po}}=2} - \eta_{i,F_{\mathrm{Po}}=1})/\eta_{i,F_{\mathrm{Po}}=1}$) as a function of the inlet dimensionless tangential velocity difference ($\hat{W}_{0,r_o}$) and Reynolds number (Re_m^*) for typical operating parameters ($F_{\mathrm{Po}} = 1$ and $F_{\mathrm{Po}} = 2$, $\gamma = 1.4$ (air), $\xi_i = 0.2$, $P_i/P_{nt} = 0.5$, choked flow)

location a the rotor inlet ($\xi = r/r_o = 1$), over time, the fluid traces an (r, θ) path through the channel between adjacent disks that is determined by integrating the differential relations

$$r d\theta = v_\theta dt \tag{3.72}$$

$$dr = v_r dt \tag{3.73}$$

Combining the above equations yields the following differential equation that can be integrated to determine the dependence of θ with r along the streamline.

$$\left(\frac{d\theta}{dr}\right)_{st} = \frac{v_\theta}{v_r r} \tag{3.74}$$

Note that since the velocities are functions only of r, the entire right side of the above equation is a function of r. In terms of the dimensionless variables described above, the streamline differential equation (3.74) can be converted to the form

$$\left(\frac{d\theta}{d\xi}\right)_{st} = -\frac{\xi + \hat{W}}{V_{ro}} \tag{3.75}$$

where V_{ro} is the ratio of radial gas velocity to rotor tangential velocity at the outer edge of the rotor

$$V_{ro} = \frac{v_{ro}}{U_o} = \frac{\dot{m}_c}{2\pi r_o b \rho_o U_o} \tag{3.76}$$

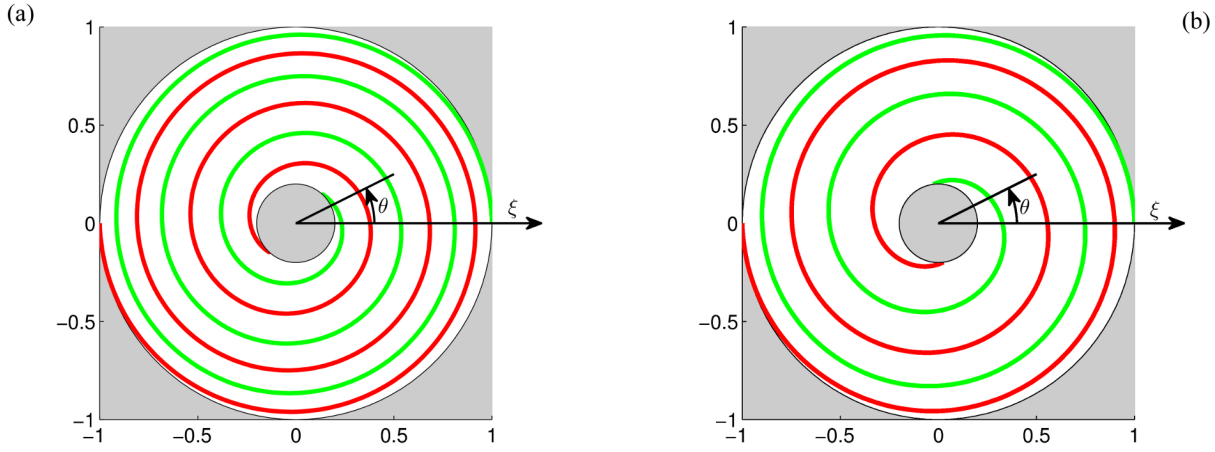

Figure 3.10: Streamlines for $\hat{W}_0 = 1.1$, $\mathrm{Re}_m^* = 5$, $\xi_i = 0.2$, and $V_{ro} = 0.05$ (a) $F_{\mathrm{Po}} = 1$ (b) $F_{\mathrm{Po}} = 2$

Rotor streamlines determined by integrating equation (3.75) for $\hat{W}_o = 3.0$, $(D_H/r_o)\mathrm{Re}_m = 5.0$, $V_{ro} = 0.05$, and $\xi_i = 0.2$ are shown in Figure 3.10. Flow along one streamline enters the rotor at $\theta = 90°$, whereas the other streamline begins at $\theta = 270°$. The model can be used to predict how the inward spiral path of the flow changes as the governing parameters are altered. Figure 3.10 shows streamlines from the roughened surfaces have a larger radial component than those generated with a smooth surface. An analytical method for predicting streamlines can be useful in designing complex disk surface geometries that consider flow direction, such as surface contours or airfoils.

3.4 Modification of the Integral Perturbation Model for Incompressible Working Fluid

The integral perturbation solution outlined above was developed for compressible working fluids, and requires slight modification to be adapted to the experimental results from a 1 cm^3 water turbine presented by Krishnan [14].

The continuity and momentum equations for flow between cylindrical channels are simplified with the following assumptions:

- laminar flow
- steady state
- incompressible flow
- axissymmetric flow
- fully developed (no entry effects)

The resulting equations are then nondimensionalized with the variables in equations 3.77 - 3.79. A parabolic velocity profile is substituted into the momentum equations, which are then integrated across the gap width. Higher order terms are then neglected based on scaling arguments. The resulting dimensionless velocity profile is shown in equation 3.81 [20].

$$\xi_i = r_i/r_o \tag{3.77}$$

$$\hat{W}_o = \frac{v_{\theta,r_o} - \omega \cdot r_o}{\omega \cdot r_o} \tag{3.78}$$

$$\mathrm{Re}_m^* = \frac{D_H \dot{m}_c}{\pi r_o^2 \mu} \tag{3.79}$$

$$P^* = \frac{\Delta P}{\rho(\omega \cdot r_o)^2} \tag{3.80}$$

$$\hat{W} = \left(\hat{W}_o - \frac{\mathrm{Re}_m^*}{24}\right) \frac{e^{\frac{20}{\mathrm{Re}_m^*}(\xi^2-1)}}{\xi} + \frac{\mathrm{Re}_m^*}{24\xi} \tag{3.81}$$

Since in [18] and [20] the flow in the rotor is already assumed to be incompressible, only the efficiency equation must be modified. Introducing the dimensionless variable P^* (equation 3.80), the rotor mechanical efficiency and the turbine isentropic efficiency are written as equations 3.82 and 3.83, respectively.

$$\eta_{rm} = 1 - \frac{(\hat{W}_i + \xi_i)\xi_i}{(\hat{W}_o + 1)} \tag{3.82}$$

$$\eta_{i,inc} = \frac{(\hat{W}_o + 1) - \xi_i(\hat{W}_i + \xi_i)}{P^*} \tag{3.83}$$

Chapter 4

Computational Fluid Dynamics (CFD) Solution of Flow Through a Tesla Turbine

4.1 Summary of ANSYS model

The purpose of the ANSYS model is to reconcile differences between the experimental data and the integral perturbation solution, and to investigate phenomena that would not otherwise be observable, such as the flow between the exit of the nozzle and the entry of the disk. Simulations were run using ANSYS/Fluent 13, with the steady, laminar solver. The flow domain modeled is bounded by a symmetry plane though the center of a gap, a symmetry plane aligned with the center of a disk, a pressure boundary exhaust at r_i, a rotating no-slip boundary at the disk face, a no slip boundary condition at the turbine case walls, and a velocity inlet boundary upstream of the nozzle entry to the case (Figure 4.1). A view of the 3D geometry from ANSYS is shown in Figure 4.2.

In this document, each combination of rotor hardware, nozzle hardware, and operating conditions are referred to by the names in the first column of Table 4.2. Table 4.2 also outlines the rotor and nozzle specifications, and the mass flow rate and rotational speed at which the rotor was tested and modeled in ANSYS.

The nozzle height, in the direction perpendicular to the turbine axis, was set based on the physical dimensions of the test hardware. The nozzle width, or the dimension parallel to the turbine axis, was not directly modeled in ANSYS because the domain repeats in the axial direction, however this nozzle dimension affects the total number of disk gaps which are exposed to flow. To assume that all disks were exposed to flow would either force the radial velocity to be too low (due to the mass flow rate being divided among a higher number of disks), or force the mass flow rate to be too high. To reconcile this, the turbine was modeled as having as many disks as would fit in the axial span of the nozzle, rounded up to the nearest integer. In ANSYS, the mass flow rate through the nozzle was set to be the total

Table 4.1: Relevant Solver Settings used in ANSYS/Fluent 13

Mesh Type	Hexahedral
Precision	Double
Solver Type	Pressure based, Steady-State
Models Used	Viscous - Laminar
Fluid	Water
Outlet Boundary Condition	0 Gauge Pressure
Pressure Outlet Backflow	From Neighboring Cell
Pressure-Velocity Coupling	Coupled
Spacial Discretization - Gradient	Green-Gauss Node Based
Spacial Discretization - Pressure	Standard
Spacial Discretization - Momentum	First Order Upwind
Solution Method	Pseudo Transient
Initialization Method	Hybrid

mass flow rate divided by the number of disks calculated in this manner, and divided by two (because each ANSYS domain is one half of a disk gap). These velocities are outlined in Table 4.2.

The efficiency is derived from the ANSYS flow field by evaluating the mass flow rate averaged tangential velocity at the inlet ($r = r_o$) and exit ($r = r_i$). These values are used to determine $\hat{W}_o$ and $\hat{W}_i$, and finally equation 3.70 or 3.83 (depending on compressible or incompressible flow through the nozzle) is used to calculate the efficiency (η_{CFD}). Note that the integral perturbation solution provides a solution to the velocity field, so substituting the ANSYS solution to velocity into equation 3.70 or 3.83 is the same as calculating the efficiency (η_{CFD}) by applying the Euler turbine equation to the flow conditions predicted by ANSYS.

When calculating η_{CFD}, the pressure drop used in the denomenator of equations 3.70 and 3.83 is the pressure drop measured experimentally, so efficiencies reported are predicted test efficiencies. In other words, in an optimized turbine design this pressure drop may be smaller, but this study is primarily concerned with analyzing the turbines that were tested experimentally.

For the purpose of recreating these results, relevant solver settings that are not obvious or documented elsewhere are listed in Table 4.1. Contour plots of the magnitude of the velocity, the tangential component of the velocity, and the radial component of the velocity, evaluated at the symmetry plane through the center of a disk gap, can be found in Appendix C.

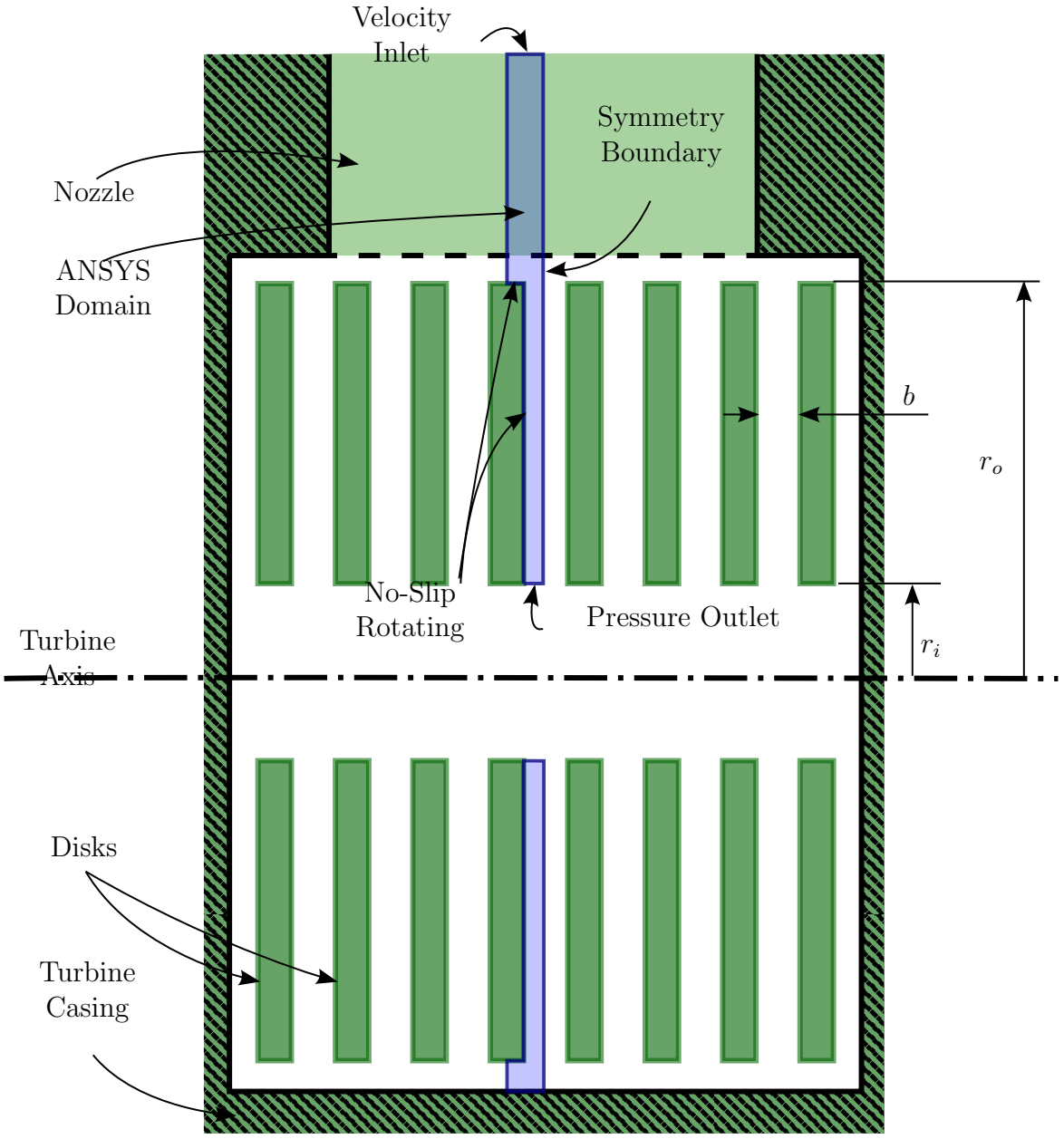

Figure 4.1: The ANSYS domain, highlighted, is bounded by a symmetry plane through the center of a gap and a symmetry plane through the center of a disk. The disk edge forms a rotating boundary. The exhaust is a pressure outlet boundary condition.

4.2 Mesh Independence Study

In order to establish insensitivity of results to mesh size, a mesh sensitivity study was performed. Since all evaluated models have similar size scales, an in-depth mesh independence study was performed on one model, specifically, with a disk gap sizing (b) of 125 μm, a nozzle exit area of 2.28 mm^2, a nozzle entrance angle of 63.5 from the radial direction, a rotational speed of 600 rad/s, and an inlet velocity of 4 m/s, or Test R1N3 (Table 4.2). The main parameters that this study is concerned with are the entrance and exit mass flow averaged tangential velocity components. In order to perform the mesh independence study, the mesh in the disk domain was held constant while the mesh in the nozzle domain was varied. Then, the mesh in the nozzle domain was held constant while the mesh in the disk domain was varied. The resulting values of inlet and exit tangential velocity, as a function of number of elements in the disk and nozzle domains, are shown in Figures 4.3 and 4.4, respectively. These same results are presented in tabular form in Table 4.2 and 4.3.

# Elements	Inlet Velocity		Exit Velocity	
in Disk	Value (m/s)	% Change	Value (m/s)	% Change
1614885	3.56720	0.08	2.5057	0.48
2462570	3.55728	0.28	2.50635	0.45
3542148	3.56426	-	2.51778	-

Table 4.2: Inlet and exit tangential velocities (mass flow averaged) vs. number of elements in the disk domain. This mesh independence study was completed on a model with $b = 125\mu m$, nozzle entrance angle of 63.5 from the radial direction, a rotational speed of 600 rad/s, and an inlet velocity of 4 m/s, or Test R1N3 (Table 4.2)

# Elements	Inlet Velocity		Exit Velocity	
in Nozzle	Value (m/s)	% Change	Value (m/s)	% Change
80115	3.55728	1.13	2.50635	0.18
177102	3.56825	0.82	2.50891	0.08
1108590	3.59785	-	2.51082	-

Table 4.3: Inlet and exit tangential velocities (mass flow averaged) vs. number of elements in the nozzle domain. This mesh independence study was completed on a model with $b = 125\mu m$, nozzle entrance angle of 63.5 from the radial direction, a rotational speed of 600 rad/s, and an inlet velocity of 4 m/s, or Test R1N3 (Table 4.2)

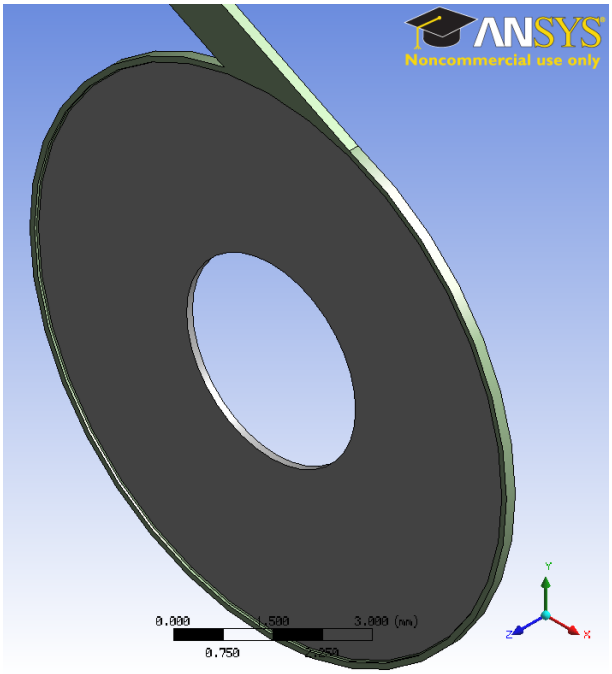

Figure 4.2: Geometry of ANSYS model

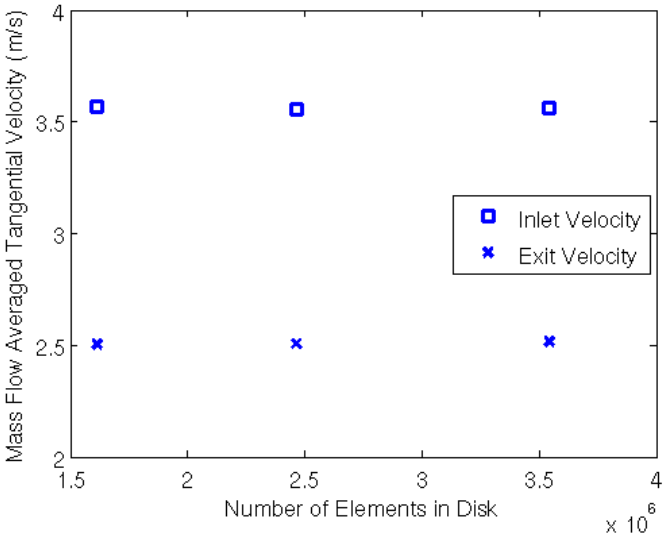

Figure 4.3: Inlet and exit tangential velocities (mass flow averaged) vs. number of elements in the disk domain. This mesh independence study was completed on a model with $b = 125\mu m$, nozzle entrance angle of 63.5 from the radial direction, a rotational speed of 600 rad/s, and an inlet velocity of 4 m/s, or Test R1N3 (Table 4.2)

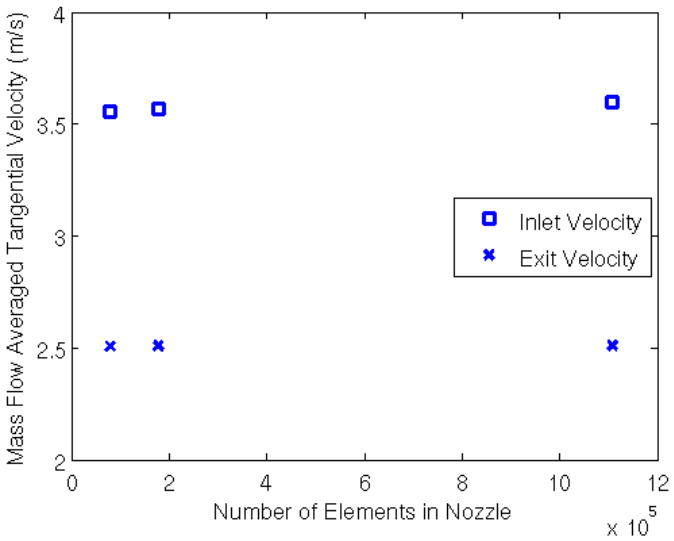

Figure 4.4: Inlet and exit tangential velocities (mass flow averaged) vs. number of elements in the nozzle domain. This mesh independence study was completed on a model with $b = 125\mu m$, nozzle entrance angle of 63.5 from the radial direction, a rotational speed of 600 rad/s, and an inlet velocity of 4 m/s, or Test R1N3 (Table 4.2)

Table 4.4: Dimensions and Operating Points of ANSYS Simulations. Test ID #s are the names used to refer to simulation results in this document. Rotor ID # and Nozzle ID # refer to those in Tables 2.1 and 2.2. Nozzle angles are measured from the radial direction.

Test ID #	Rotor ID #	# of Disks	Gap Size (b) (μm)	Nozzle ID #	Nozzle Angle (degrees)	Mass Flow Rate (g/s)	Nozzle Inlet Velocity (m/s)	Rotational Speed (RPM)	Efficiency (η_{CFD}) (%)
R1N3	1	20	125	3	63.5	10	4	5760	33.0
R1N4-1	1	20	125	4	63.5	12	3.43	6020	28.8
R1N4-2	1	20	125	4	63.5	3	0.857	528	18.3
R1N4-3	1	20	125	4	63.5	12	3.43	5500	25.4
R1N7	1	20	125	7	52.7	12	1.5	5070	11.5
R3N3	3	13	250	3	63.5	10	3.82	5770	36.2
R3N4	3	13	250	4	63.5	12	3.2	5110	24.4

Chapter 5

Discussion

First, the integral perturbation solution will be compared with ANSYS simulations and experimental data for a 73 mm diameter air turbine [18]. Next, the same analysis is compared with ANSYS simulations and experimental data for a 10 mm diameter turbine running water. In both cases, the ability of the integral perturbation solution to predict turbine efficiency will be assessed. Trends in performance will be analyzed, specifically, the effect of disk spacing and nozzle design will be examined to the extent possible with the available data.

5.1 Comparison to Test Data from a 73 mm Air Tesla Turbine

A comparison with previous experimental data[18] can be seen in Table 5.1. The agreement between test data and the integral perturbation solution efficiency is reasonable considering the uncertainty of the test data, and is similar to the accuracy of the earlier model developed by Carey[2]. These same efficiencies are plotted in Figure 5.1. The experimental efficiency deviates from the value predicted by the integral perturbation solution by an average of 29%, a minimum of 5.4%, and a maximum of 52%.

Figure 5.2 shows a 3D plot of turbine efficiency as a function of Re_m^* and $\hat{W}_{0,r_o}$ for the operating parameters in the first four lines of table 5.1. The data points are overlaid on top of the surface plot, which shows how the data compares to the predictions of efficiency. The figure shows that the integral perturbation solution correctly predicts that decreasing $\hat{W}_{0,r_o}$ will increase efficiency, and suggests that decreasing both Re_m^* and $\hat{W}_{0,r_o}$ can dramatically improve performance.

A 3D plot of turbine efficiency with typical operating parameters, and over ideal ranges of Re_m^* and $\hat{W}_{0,r_o}$, is shown in Figure 5.3. At very low values of Re_m^* and $\hat{W}_{0,r_o}$, the analysis shows that very high turbine efficiencies, above 75%, can be achieved. Practical issues arise when generating power in microchannels such as these at very low values of $\hat{W}_{0,r_o}$ and Re_m^*. Reducing $\hat{W}_{0,r_o}$ requires the rotor to be spinning at speeds very close to the air inlet speeds. This is difficult to achieve because it requires very low rotor torque and high speeds, which

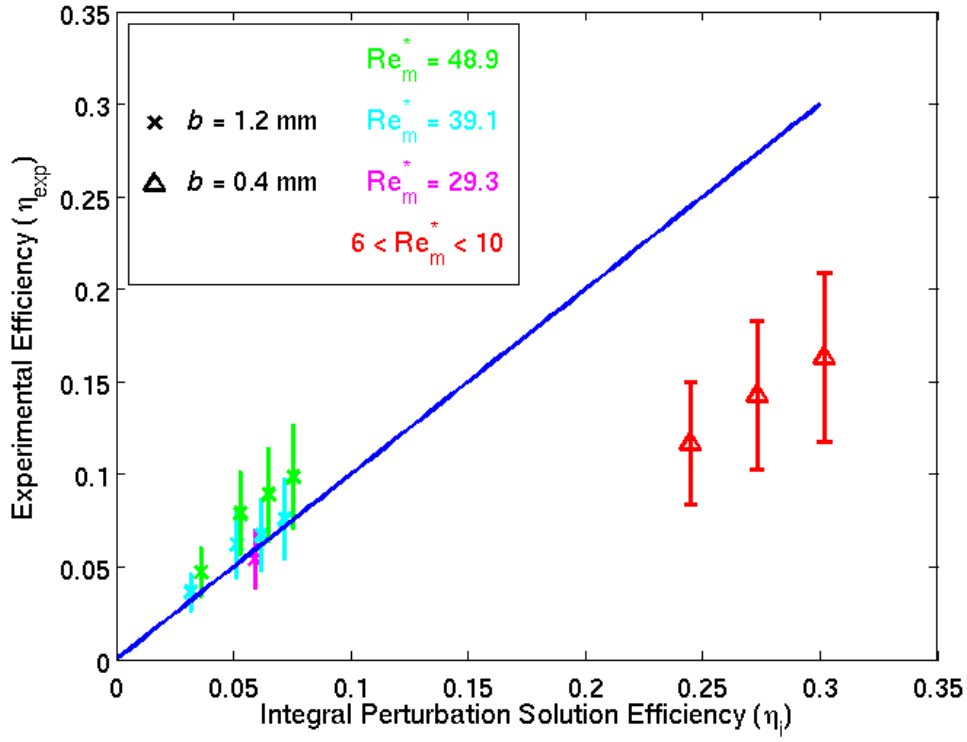

Figure 5.1: Efficiency predicted by the integral perturbation solution vs. experimental efficiency of a 73 mm diameter air turbine. The blue line represents the unity slope, or a match between experimental and integral perturbation efficiencies. The efficiency values plotted here are taken from Table 5.1. The experimental efficiency deviates from the value predicted by the integral perturbation solution by an average of 29%, a minimum of 5.4%, and a maximum of 52%.

may require high gear ratios to achieve in some applications. Also, lower Reynolds numbers require very small disk spacings (b) and larger disk radii (r_o).

5.2 Comparison to Test Data and CFD Simulations of a 10 mm Water Tesla Turbines

An important conclusion to be made from the data generated is the trends in performance with design parameters. To the extent possible with the limited set of turbine configurations, trends in performance are analyzed.

First, decreasing interdisk space b increases efficiency. This is observed in ANSYS, test data, and the integral perturbation solution (Figure 5.5). This can be attributed to the

Table 5.1: Comparison of Analysis with Experimental Data from Romanin et al.[18].

b mm	Re_m^*	$\hat{W}_{0,r_o}$	M_o	$(P_i/P_{nt})_{exp}$	η_{exp} (%)	η_i (%)
1.2	29.3	13.6	0.068	0.49	5.4	5.9
1.2	39.1	18.2	0.052	0.43	3.6	3.2
1.2	39.1	10.0	0.091	0.40	6.2	5.1
1.2	39.1	8.1	0.11	0.40	6.7	6.2
1.2	39.1	6.8	0.128	0.40	7.6	7.2
1.2	48.9	11.2	0.082	0.37	4.7	3.6
1.2	48.9	6.8	0.128	0.34	7.9	5.3
1.2	48.9	5.3	0.158	0.34	8.9	6.5
1.2	48.9	4.4	0.184	0.34	9.9	7.5
0.4	6.6	5.4	0.156	0.51	11.7	24.4
0.4	8.3	3.5	0.221	0.47	14.3	27.3
0.4	9.9	2.4	0.291	0.46	16.3	30.2

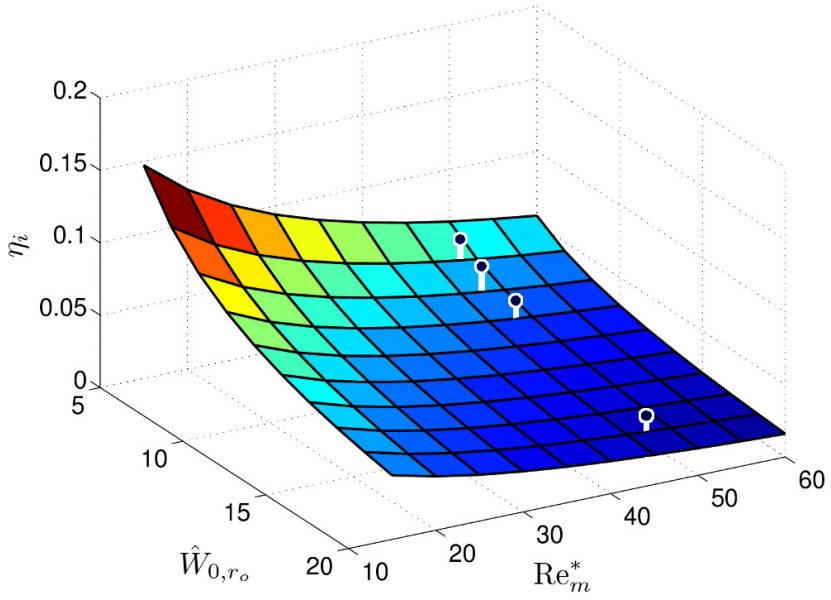

Figure 5.2: A plot of experimental data from the first four lines of table 5.1 with a surface plot of efficiency (η_i) from eq. (3.71) ($F_{\mathrm{Po}} = 1$ (smooth wall), $\gamma = 1.4$ (air), $\xi_i = 0.45$, $P_i/P_{nt} = 0.4$, choked flow).

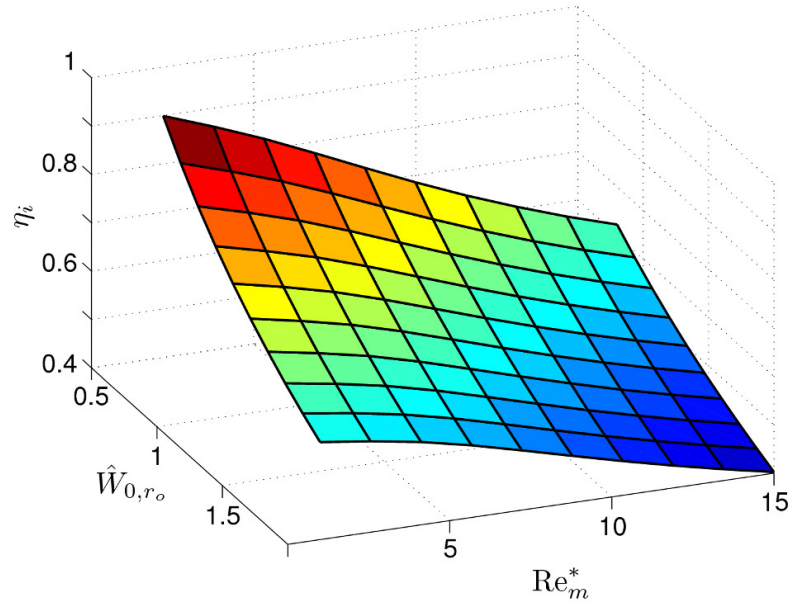

Figure 5.3: A plot of efficiency (η_i) as a function of dimensionless tangential velocity difference at the inlet ($\hat{W}_{0,r_o}$) and modified Reynolds number (Re_m^*) for typical operating conditions: $F_{\mathrm{Po}} = 1$ (smooth wall), $\gamma = 1.4$ (air), $\xi_i = 0.2$, $P_i/P_{nt} = 0.5$, choked flow.

increase in Reynolds number, or in other words, increasing the viscous forces in the flow which are responsible for momentum transfer from the fluid to the disks. In this analysis, total mass flow rate ($\dot{m}$) and radial velocity are held constant, while the number of disks and disk spacing (b) are varied.

Increasing the velocity at the inlet to the rotor by decreasing the nozzle area (preserving mass flow rate) increases efficiency. This is observed in ANSYS, test data, and the integral perturbation solution (Figure 5.6). Operation of the Tesla turbine relies on converting a pressure head to kinetic energy, which is then transfered to the rotor, so a higher fluid velocity increases efficiency. This must be done while minimizing pressure losses in the nozzle due to friction.

Correlation of Experimental Data with Integral Perturbation Solution

For all simulations run in ANSYS, the experimental efficiency vs. predicted efficiency is shown in Figure 5.4. This graph shows a strong correlation between the experimental and predicted efficiencies. The experimental efficiency deviates from the value predicted by the integral perturbation solution by an average of 52%, a minimum of 4.5%, and a maximum

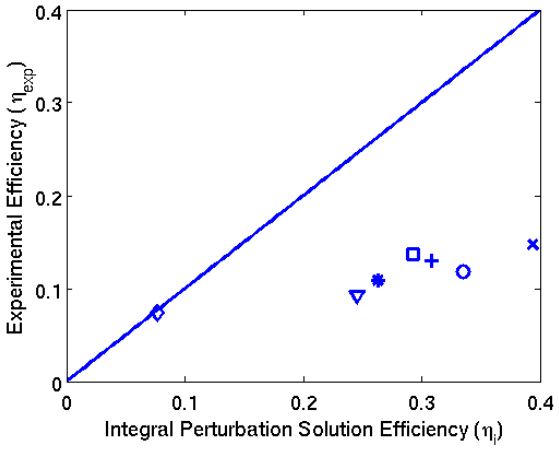

	Gap Size (b) (μm)	Nozzle Inlet Velocity (m/s)	Speed (RPM)	Mass Flow Rate (g/s)
×	125	4	5760	10
+	125	3.43	6020	12
✱	125	0.857	528	3
□	125	3.43	5500	12
◇	125	1.5	5070	12
○	250	3.82	5770	10
▽	250	3.2	5110	12

Figure 5.4: Efficiency predicted by the integral perturbation solution vs. experimental efficiency. The experimental efficiency deviates from the value predicted by the integral perturbation solution by an average of 52%, a minimum of 4.5%, and a maximum of 65%.

of 65%. As the predicted analysis uses the experimental head and RPM, and since friction losses are accounted for in the experimental results, nozzle loss and bearing friction are not the cause of the deviation between the experimental and the predicted efficiencies. The deviation between these is attributed to volume loss due to poor sealing and experimental uncertainty. Additionally, the moment of inertia of the rotor during deceleration may be underestimated due to the entrapped fluid inside the rotor.

Comparison of ANSYS model to the Integral Perturbation Solution and Experimental Data

The inlet tangential turbine velocity, or the velocity at the outer radius of the rotor, can be calculated in several different ways. First, the inlet tangential velocity can be calculated as the component of the nozzle exit velocity vector that is in the tangential direction, or $v_{\theta,r_o} = v_{noz}\sin(\theta)$, where θ is the angle between the nozzle direction and the radial direction. This method gives a reasonably good correlation between integral perturbation solution efficiency and ANSYS efficiency (Figure 5.10).

Alternatively, the kinetic energy of the fluid at the exit of the nozzle can be conserved, and the radial component of the flow can be calculated based on mass flow rate considerations. In other words, $v_{\theta,r_o} = \sqrt{v_{noz}^2 - v_r^2}$, where v_r is set to the radial velocity required for the given mass flow rate. This would be more appropriate if the flow changes direction after it exits the nozzle due to interactions with the turbine casing. The correlation between ANSYS efficiencies and integral perturbation solution efficiencies improves slightly when using this method (Figure 5.11). These two methods, however, do not change the value for inlet tangential velocity considerably. Other factors that are difficult to predict, such as the constriction effect of the finite disk thickness, also have an effect on the inlet tangential

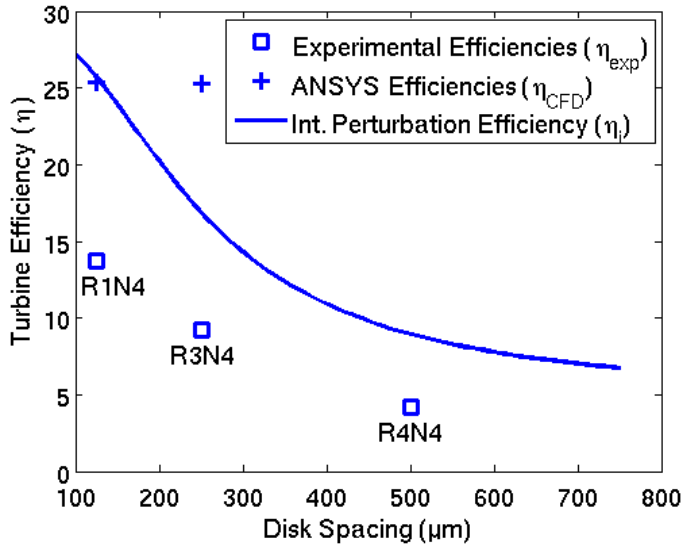

Figure 5.5: Efficiency vs. disk gap (b) plotted for the same system with all ANSYS and experimental data points plotted, as well as the trend predicted by the integral perturbation solution. The rotors and nozzles for the experimental and ANSYS results are indicated.

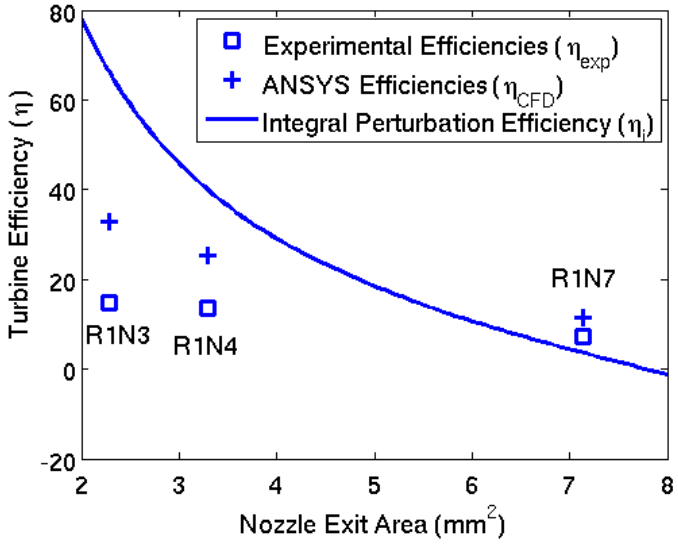

Figure 5.6: Efficiency vs. nozzle exit area. By increasing the fluid velocity while holding the mass flow rate constant, the efficiency is increased. This trend is predicted by the test data, ANSYS, and the integral perturbation solution. The rotors and nozzles for the experimental and ANSYS results are indicated.

velocity.

For the sake of comparison with the ANSYS model, the inlet tangential velocity ($\hat{W}_o$) can also be set to the velocity predicted by ANSYS. To accomplish this, the mass-flow averaged tangential velocity at the outer radius of the rotor ($r = r_o$) is taken from the ANSYS solution, and this value is used to calculate the value of $\hat{W}_o$. This separates flow entry issues, which are not modeled by the integral perturbation solution, and allows a comparison of the velocity profile in the rotor as predicted by ANSYS and the velocity profile predicted by the integral perturbation solution. The correlation between the ANSYS efficiency and integral perturbation solution efficiency again improves slightly when using this method (Figure 5.12). This indicates that the integral perturbation solution accurately predicts the physics of the flow inside the rotor, and small inaccuracies can be produced if the flow from the exit of the nozzle to the entry of the disk is not treated properly.

Plots of circumferentially averaged nondimensional tangential relative velocity vs. radius for the integral perturbation solution and the ANSYS solution are shown in Figure 5.7. The integral perturbation solution matches the ANSYS results inside the rotor (in other words, when the inlet velocity of the integral perturbation solution is set equal to the rotor inlet velocity from ANSYS). This is true even though the integral perturbation solution assumes axial symmetry while the flow in ANSYS is injected through a nozzle with a finite arc length.

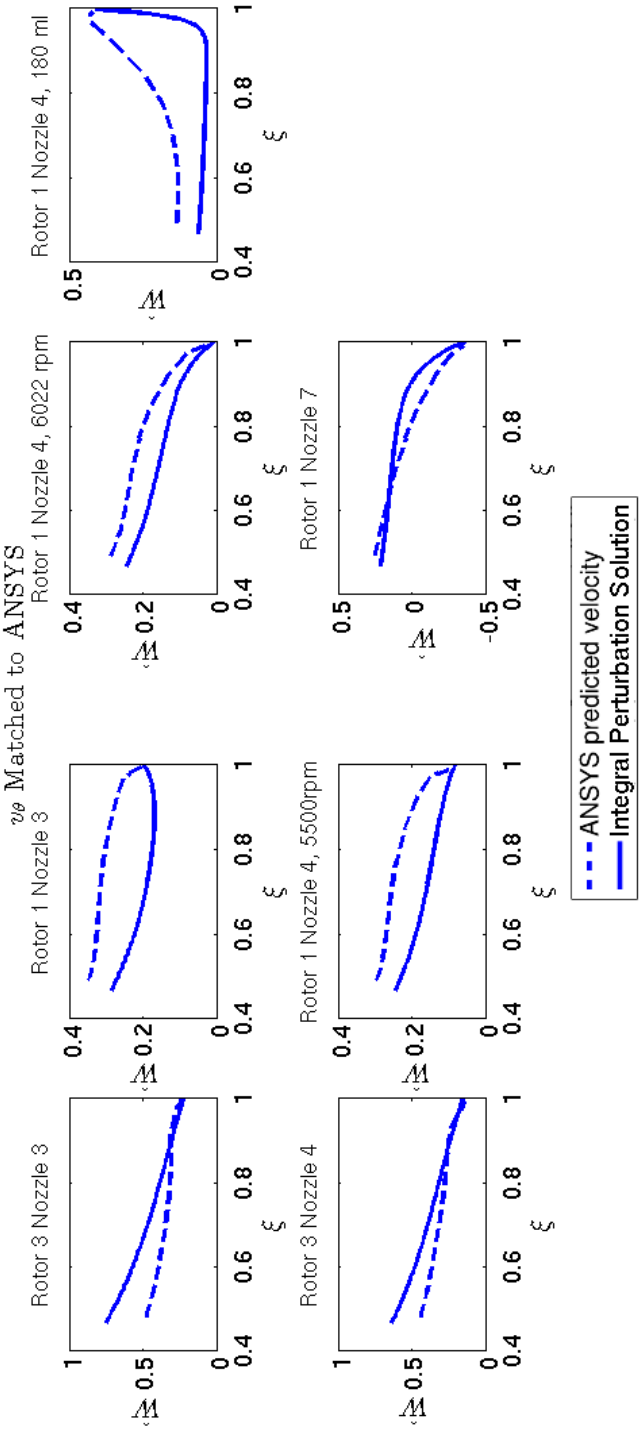

Figure 5.7: Nondimensional rotor velocities vs. nondimensional radial coordinate as predicted by the integral perturbation solution (solid line) and ANSYS (dashed). The inlet tangential velocity used to calculate the velocity profile in the integral perturbation solution is set equal to the one predicted by ANSYS.

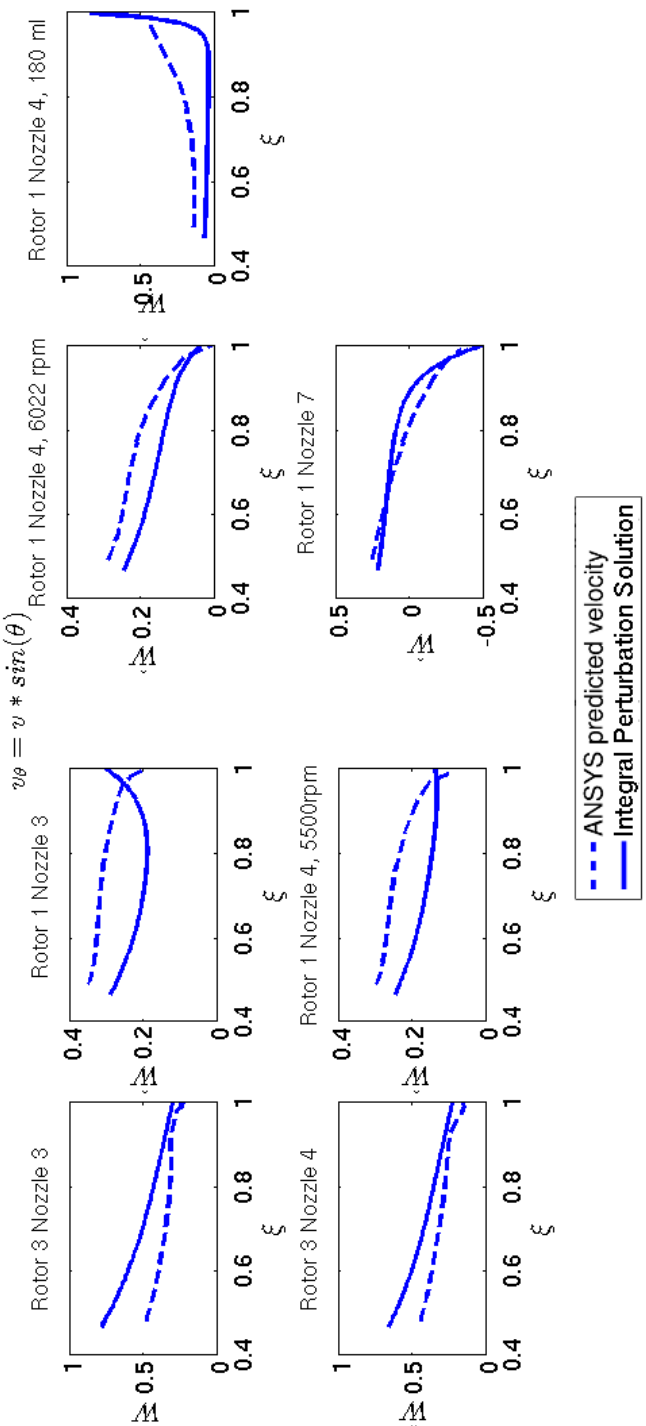

Figure 5.8: Nondimensional rotor velocities vs. nondimensional radial coordinate as predicted by the integral perturbation solution (solid line) and ANSYS (dashed). The inlet tangential velocity used to calculate the velocity profile in the integral perturbation solution is based on the nozzle angle.

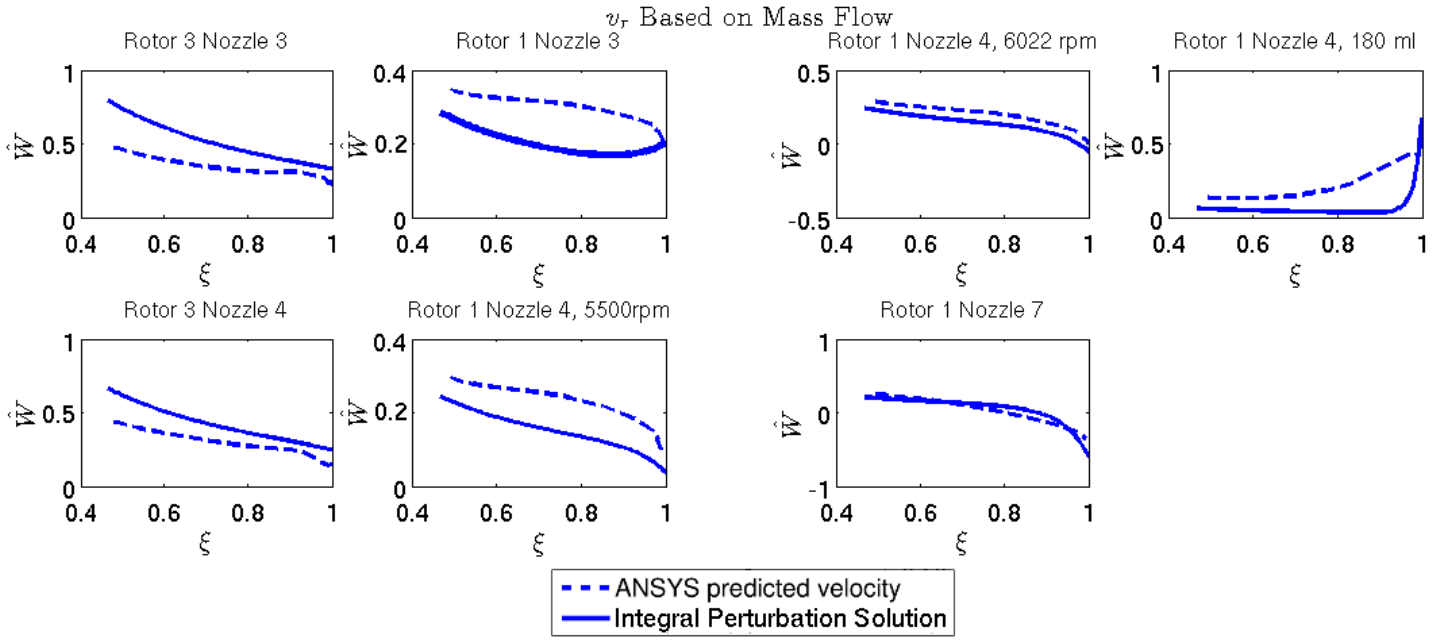

Figure 5.9: Nondimensional rotor velocities vs. nondimensional radial coordinate as predicted by the integral perturbation solution (solid line) and ANSYS (dashed). The inlet tangential velocity used to calculate the velocity profile in the integral perturbation solution is calculated by setting the total magnitude of the velocity ($\sqrt{v_\theta^2 + v_r^2}$) equal to the magnitude at the exit of the nozzle. v_r is calculated based on the mass flow rate through the rotor.

Comparison of Axisymmetric and Non-Axissymmetric Velocity Fields

One assumption of the integral perturbation solution is that the flow can be modeled as axisymmetric (independent of θ, or $v = v(r, z)$). Although the integral perturbation solution has been shown to agree very well with efficiencies predicted by ANSYS (Figures 5.7 - 5.12), an axisymmetric simulation can be easily modeled in ANSYS. For two different ANSYS simulations (R1N4-1 and R1N3, see Table 4.2), the nozzle domain was suppressed, leaving only the disk domain, and the velocities at the inlet of the disk domain were set to be equal to those in the same model with the nozzle included. In other words, the tangential velocity at the outer radius of the disk gap was set to the mass-flow rate averaged tangential velocity at the same location in the full ANSYS simulation. The radial velocity was set so that the mass flow rate through the turbine was equivalent in both models. The result is an ANSYS simulation that has an axisymmetric flow field, but is otherwise the same as the ANSYS simulation with the nozzle included. Figure 5.13 and 5.14 show the dimensionless tangential velocity difference ($\hat{W}$) as a function of dimensionless radius (ξ) for both the ANSYS axisymmetric and ANSYS non-axisymmetric case, as well as the velocity prediction of the integral perturbation solution, for two different hardware configurations (R1N4-1 and R1N3, see Table 4.2). These plots shows that the mass flow averaged tangential velocity ($\hat{W}$) approaches the axisymmetric solution as radius decreases, with the exit velocity differing by 6% between the two cases in Figure 5.13 and with nearly equivalent exit velocities in 5.14. This reinforces that the assumption of axisymmetry made in the integral perturbation solution is reasonable, and the model is still useful in analyzing turbines without axisymmetric nozzles, as occurs in most Tesla turbine hardware.

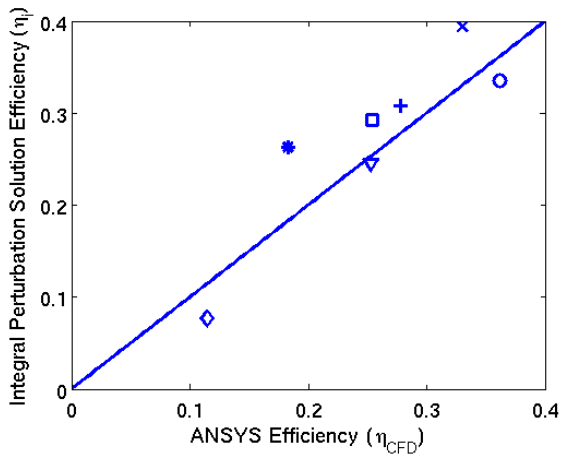

	Gap Size (b) (μm)	Nozzle Inlet Velocity (m/s)	Speed (RPM)	Mass Flow Rate (g/s)
×	125	4	5760	10
+	125	3.43	6020	12
✱	125	0.857	528	3
□	125	3.43	5500	12
◇	125	1.5	5070	12
○	250	3.82	5770	10
▽	250	3.2	5110	12

Figure 5.10: Efficiency predicted by the integral perturbation solution vs. the efficiency predicted by ANSYS, with a line of unity slope. The inlet velocities are calculated as the magnitude of the nozzle exit velocity, times the sine of the angle of the nozzle. The rotors and nozzles used in each test are indicated by the numbers following R and N in the legend, respectively. Three different operating points were tested for the combination of rotor 1 and nozzle 4. The efficiency predicted by ANSYS deviates from the value predicted by the integral perturbation soultion by an average of 18%, a minimum of 0.7%, and a maximum of 50%.

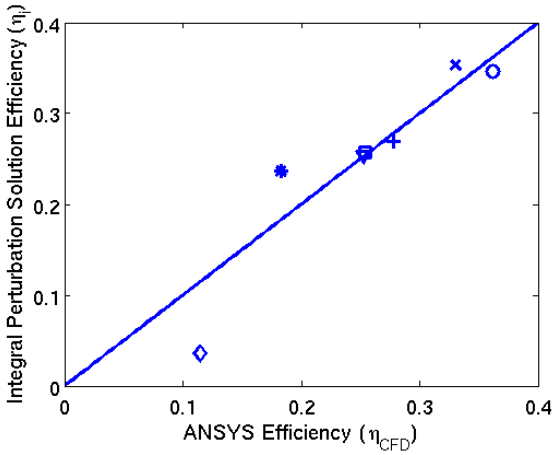

	Gap Size (b) (μm)	Nozzle Inlet Velocity (m/s)	Speed (RPM)	Mass Flow Rate (g/s)
×	125	4	5760	10
+	125	3.43	6020	12
✱	125	0.857	528	3
□	125	3.43	5500	12
◇	125	1.5	5070	12
○	250	3.82	5770	10
▽	250	3.2	5110	12

Figure 5.11: Efficiency predicted by the integral perturbation solution vs. the efficiency predicted by ANSYS, with the inlet velocity (v_{θ,r_o}) predicted by setting the radial velocity (v_r) based on mass flow considerations, and calculating the tangential component. The rotors and nozzles used in each test are indicated by the numbers following R and N in the legend, respectively. Three different operating points were tested for the combination of rotor 1 and nozzle 4. The efficiency predicted by ANSYS deviates from the value predicted by the integral perturbation solution by an average of 37%, a minimum of 1.3%, and a maximum of 220%.

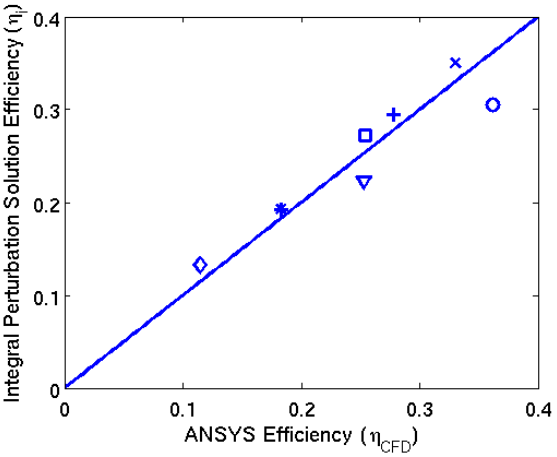

	Gap Size (b) (μm)	Nozzle Inlet Velocity (m/s)	Speed (RPM)	Mass Flow Rate (g/s)
×	125	4	5760	10
+	125	3.43	6020	12
✱	125	0.857	528	3
□	125	3.43	5500	12
◇	125	1.5	5070	12
○	250	3.82	5770	10
▽	250	3.2	5110	12

Figure 5.12: Efficiency predicted using the integral perturbation solution vs. the efficiency predicted by ANSYS, using v_{θ,r_o} as predicted by ANSYS. The rotors and nozzles used in each test are indicated by the numbers following R and N in the legend, respectively. Three different operating points were tested for the combination of rotor 1 and nozzle 4. The efficiency predicted by ANSYS deviates from the value predicted by the integral perturbation solution by an average of 10%, a minimum of 3.9%, and a maximum of 23%.

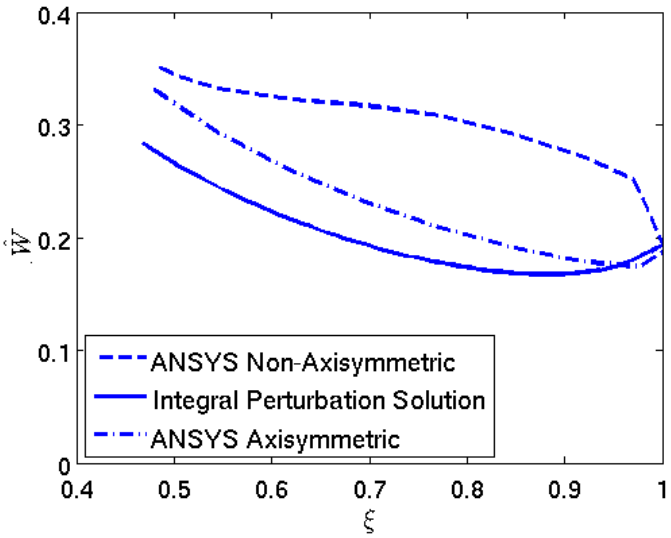

Figure 5.13: For Rotor 1 and Nozzle 3, the flow field is plotted using the integral perturbation solution, an axisymmetric ANSYS simulation, and a non-axisymmetric ANSYS simulation. The axisymmetric ANSYS simulation is modeled by setting the inlet velocity to the disk gap as uniformly equal to the mass flow averaged tangential velocity in the full (non-axisymmetric) simulation, and setting the total mass flow rate through the gap as equal. The flow field is closely approximated by assuming that the velocity is independent of θ, the value of $\hat{W}$ at the exit ($r = r_i$) varies by 6%.

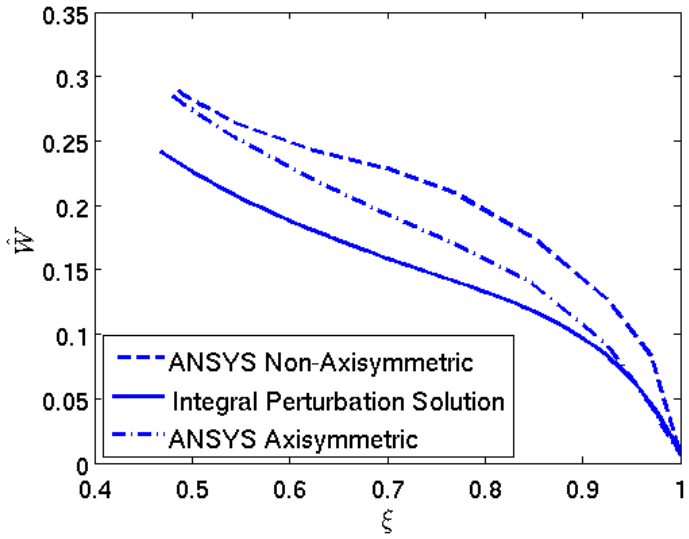

Figure 5.14: For Rotor 1 and Nozzle 4, the flow field is plotted using the integral perturbation solution, an axisymmetric ANSYS simulation, and a non-axisymmetric ANSYS simulation. The axisymmetric ANSYS simulation is modeled by setting the inlet velocity to the disk gap as uniformly equal to the mass flow averaged tangential velocity in the full (non-axisymmetric) simulation, and setting the total mass flow rate through the gap as equal. The flow field is closely approximated by assuming that the velocity is independent of θ, the value of $\hat{W}$ at the exit ($r = r_i$) is nearly equal.

Chapter 6

Conclusions

It has been shown that the use of an integral perturbation analysis scheme allows construction of a series expansion solution of the governing equations for rotating microchannel flow between the rotor disks of a Tesla-type drag turbine. Several useful advantages of the integral perturbation solution have been shown. One is that it provides a rigorous approach that retains the full complement of momentum and viscous effects to consistent levels of approximation in the series solution. Another is that by constructing the solution in dimensionless form, the analysis directly indicates all the dimensionless parameters that dictate the flow and transport, and, in terms of these dimensionless parameters, it provides a direct assessment of the relative importance of viscous, pressure and momentum effects in different directions in the flow. The analysis also indicated that closed form equations can be obtained for the lowest order contribution to the series expansion solution, and the higher order term contributions are very small for conditions of practical interest. This provides simple mathematical relations that can be used to compute the flow field velocity components and the efficiency of the turbine, to very good accuracy, from values of the dimensionless parameters for the design of interest.

In addition, it has been demonstrated here that this solution formulation facilitates modeling of enhanced rotor drag due to rotor surface microstructuring. The type of drag turbine of interest here is one of very few instances in which enhancement of drag is advantageous in fluid machinery. We have demonstrated that by parameterizing the roughness in terms of the surface Poiseuille number ratio (F_{Po}), the integral perturbation solution developed here can be used to predict the enhancing effect of rotor surface microstructuring on turbine performance for a wide variety of surface microstructure geometries.

While the integral perturbation solution models the inlet flow as being uniform over the outer perimeter of the disk. Real turbines of this type have a discrete number of nozzles that deliver inlet flow at specific locations. This idealization has been evaluated to the extent possible using turbine CFD simulations in ANSYS, and it has been shown that the tangential velocity of the axisymmetric and non-axisymmetric simulations matches at the turbine exit, in other words the mismatch between the two is confined to an area close to the inlet, and the effect of assuming axisymmetry is minimal for the cases analyzed.

For both sets of test data that were compared to the integral perturbation solution predictions, the efficiencies predicted over the range of parameters tested correlate strongly with experimental results. The experimental results of the 10 mm diameter water turbine deviated from the integral perturbation solution predictions by an average of 52%. The experimental results of the 73 mm diameter air turbine deviated from the integral perturbation solution predictions by an average of 29%. In both cases, proper prediction of inlet tangential velocity that is delivered by the nozzle has been identified as a major contributor to the discrepancy between experimental results and integral perturbation solution predictions. This conclusion is supported by the fact that the deviation of ANSYS predicted efficiencies improves from an average of 18% to an average of 10% among the 10 mm diameter water turbine simulations when the nozzle entry considerations are bypassed by matching the rotor inlet velocity in the integral perturbation solution to that predicted by ANSYS. In the air turbine, incorrect rotor inlet velocity specification is likely to be a larger contributor to the deviation between experimental results and integral perturbation solution results, because the angle of the nozzle was not known.

Additionally, the consequences of the flow impinging on the edge of the disk and flow leakage between the turbine rotor and case were not assessed, but may have contributed to the discrepancy between experimental results and integral perturbation solution predictions. The three reasons for under-performing test hardware listed here, namely, improper inlet velocity specification, disk edge flow impingement, and flow losses can all be mitigated with an optimized Tesla design. Additionally, the pressure drop used in the integral perturbation model was the same as that measured experimentally. The flow losses through the turbine (aside from the rotor) were not optimized in these experimental devices, and careful design of nozzles and exhausts can lead to a lower overall pressure drop in a similar turbine design and thus a higher efficiency.

The experimental data collected does not allow observation of the flow field inside the rotor to compare to the integral perturbation solution of flow in the rotor. This is due to the fact that the integral perturbation solution domain is the rotor disk gap only, while experiments evaluated performance of the entire Tesla device. Based on the previous discussion of the agreement between the ANSYS CFD solutions and the integral perturbation solutions, the discrepancies between the experimental data (η_{exp}) and the integral perturbation solution efficiencies (η_i) has been attributed to factors external to the rotor gap (disk edge impingement, flow loss, poor nozzle design, incorrect inlet velocity predictions). The integral perturbation solution could be more carefully analyzed by an experiment designed to evaluate the flow field in the rotor, instead of an entire Tesla device.

In both sets of test data, all important design trends predicted by the integral perturbation solution were demonstrated experimentally. Specifically, decreasing the gap size and increasing the rotor inlet velocity were shown to increase turbine efficiency. These results can be used to conclude that the integral perturbation solution accurately predicts flow in the turbine rotor and can be used to provide design guidance, and that special care should be taken to appropriately estimate rotor inlet velocity.

The integral perturbation solution has been used to project high efficiency Tesla tur-

bine designs. Low Reynolds numbers and high rotor speeds result in the highest turbine isentropic efficiencies. Specifically, for modified Reynolds numbers (Re_m^*) less than 1.2 and dimensionless inlet velocity difference ($\hat{W}_0$) less than 1.2 (or $M_o > 0.41$ for choked flow), efficiencies up to and exceeding 80% can be achieved. In addition to low Reynolds numbers and high rotor speeds, roughened or microstructured surfaces can provide efficiency benefits that can further improve turbine performance. Surface roughness was shown to improve turbine efficiency by 9.2% in one example case.

The results of this investigation clearly indicate a path of design changes that can significantly improve the energy efficiency performance of Tesla-type disk-rotor drag turbines. The trends that indicate this path are supported by available experimental data.

Appendix A

Derivation of Integral Solution of Flow Through Tesla Rotor

Here the derivations to the equations derived in Chapter 3 are presented in greater detail.

A.1 Derivation of Velocity Profile as a Function of Radius ($\hat{W} = f(\xi)$)

The radial velocity profile (equation 3.30 and 3.31) derivation is comparatively simple and is outlined in sufficient detail in Chapter 3. The tangential velocity profile is outlined here. Beginning with the θ-direction momentum equation, assuming steady, laminar, axisymmetric flow, without body forces (e.g. gravity) and neglecting entry and exit effects, we have equation 3.12 from Chapter 3, reproduced here in Equation A.1.

$$v_r \frac{\partial v_\theta}{\partial r} + \frac{v_r v_\theta}{r} = \nu \left\{ \frac{1}{r} \frac{\partial}{\partial r} \left(r \frac{\partial v_\theta}{\partial r} \right) + \frac{\partial^2 v_\theta}{\partial z^2} - \frac{v_\theta}{r^2} \right\} \tag{A.1}$$

Next, several substitutions must be made. From the postulated velocity profile and the definition of $\hat{W}$ (equations 3.15 and 3.35), we can write equation A.2.

$$v_\theta = U_o \phi \hat{W} + U(r) \tag{A.2}$$

From the radial velocity equations (3.14, 3.30, and 3.31) and the definition of Re_m^* (equation 3.57), we can write equation A.3.

$$v_r = -\mathrm{Re}_m^* \frac{\nu \phi}{2b\xi\varepsilon} \tag{A.3}$$

Finally, from the definition of ξ (equation 3.34), we can write equation A.4.

$$r = r_o \xi \tag{A.4}$$

Substituting equations A.2 - A.4 into the momentum equation equation A.1 and simplifying results in equation A.5.

$$-\frac{r_o^2 \mathrm{Re}_m^*}{2brD_H}(\phi^2\hat{W}' + \frac{2\phi}{r_o} + \phi^2\frac{\hat{W}}{r}) = \frac{\phi}{r}\hat{W}' + \phi\hat{W}'' + \hat{W}\phi'' - \phi\frac{\hat{W}}{r^2} \tag{A.5}$$

Where $\hat{W}'$ and $\hat{W}''$ are derivatives with respect to the dimensionless radius ξ (equations A.6 and A.7), and ϕ'' is the second derivative with respect to z, given in equation A.8.

$$\hat{W}' = \frac{d\hat{W}}{d\xi} \tag{A.6}$$

$$\hat{W}'' = \frac{d^2\hat{W}}{d\xi^2} \tag{A.7}$$

$$\phi'' = \frac{d^2\phi}{dz^2} \tag{A.8}$$

Next, the entire equation is integrated over the gap width in the z direction, in other words, from $z = -b/2$ to $z = b/2$. The integrations of the dimensionless velocity profile ϕ, ϕ^2, and ϕ'', from $-b/2$ to $b/2$, are given in equations 3.27, 3.32, and 3.33 respectively. This results in equation A.9.

$$-\frac{r_o^2 \mathrm{Re}_m^*}{2brD_H}\left(\frac{2(n+1)}{2n+1}b\hat{W}' + \frac{2b}{r_o} + \frac{2(n+1)}{2n+1}b\frac{\hat{W}}{r}\right) = \frac{b}{r}\hat{W}' + b\hat{W}'' - \frac{4(n+1)}{b}\hat{W} - b\frac{\hat{W}}{r^2} \tag{A.9}$$

Further simplifying this equation by substituting in the definition of ε ($\varepsilon = 2b/r_o$, equation 3.38) and by grouping multipliers on $\hat{W}$, $\hat{W}'$, and $\hat{W}''$ on the right hand side results in equation 3.41. The remaining analysis, grouping terms by the ε multiplier and arguments for neglecting higher order terms, and finally solving for the 0th order solution, is outlined in sufficient detail in chapter 3.

A.2 Derivation of Dimensionless Pressure Profile as a Function of Dimensionless Radius ($\hat{P}(\xi)$)

Beginning with the r-direction momentum equation, assuming steady, laminar, axisymmetric flow, without body forces (e.g. gravity) and neglecting entry and exit effects, we have equation 3.11 from Chapter 3, reproduced here in Equation A.10.

$$v_r\frac{\partial v_r}{\partial r} - \frac{v_\theta^2}{r} = -\frac{1}{\rho}\left(\frac{\partial P}{\partial r}\right) + \nu\left\{\frac{1}{r}\frac{\partial}{\partial r}\left(r\frac{\partial v_r}{\partial r}\right) + \frac{\partial^2 v_r}{\partial z^2} - \frac{v_r}{r^2}\right\} \tag{A.10}$$

Similar to the solution of the θ-direction momentum equation, we introduce the postulated velocity profiles in the θ and r directions (equations 3.15 and 3.14) and the definition

of $\hat{W}$ (equations 3.14 and 3.35). In addition, to solve the r-direction momentum equation we define V_{ro} and $\hat{P}$ (equations 3.37 and 3.36). Substituting these non-dimensional parameters into equation A.10 results in equation A.11.

$$\frac{\partial \hat{P}}{\partial \xi} = \hat{P}' = 2\frac{V_{ro}^2\phi^2}{\xi^3} + 2\frac{\phi^2\hat{W}^2}{\xi} + 4\phi\hat{W} + 2\xi - \frac{2V_{ro}\phi''r_o\nu}{U_o\xi} \tag{A.11}$$

Next, equation A.11 must be integrated. Recalling the integrations of the dimensionless velocity profile ϕ, ϕ^2, and ϕ'', from $-b/2$ to $b/2$, (equations 3.27, 3.32, and 3.33), gives equation A.12.

$$\hat{P}'b = 2\frac{V_{ro}^2 b}{\xi^3}\frac{2(n+1)}{2n+1} + 2\frac{\hat{W}^2 b}{\xi}\frac{2(n+1)}{2n+1} + 4\hat{W}b + 2\xi b + 2\frac{V_{ro}r_o\nu}{U_o\xi}\frac{4(n+1)}{b} \tag{A.12}$$

Equation A.12 can be rearranged to equation 3.40.

Appendix B

Summary of Experimental Data for the 73 mm Air Turbine

Table B.1: Comparison of Analysis with Experimental Data from Romanin et al.[18].

b (mm)	Flow Rate (scfm)	Re_m^*	$\hat{W}_{0,r_o}$	ω (rpm)	M_o	$P_{nt,exp}$ (kPa)	$P_{i,exp}$ (kPa)	$(P_i/P_{nt})_{exp}$	$\eta_{i,exp}$ (%)	$\eta_{i,model}$ (%)
1.2	15	29.3	13.6	5605	0.068	247	120	0.49	5.4	5.9
1.2	20	39.1	18.2	4300	0.052	310	132	0.43	3.6	3.2
1.2	20	39.1	10.0	7485	0.091	334	132	0.40	6.2	5.1
1.2	20	39.1	8.1	9100	0.11	333	132	0.40	6.7	6.2
1.2	20	39.1	6.8	10600	0.128	332	132	0.40	7.6	7.2
1.2	25	48.9	11.2	6760	0.082	414	152	0.37	4.7	3.6
1.2	25	48.9	6.8	10560	0.128	445	152	0.34	7.9	5.3
1.2	25	48.9	5.3	13080	0.158	441	152	0.34	8.9	6.5
1.2	25	48.9	4.4	15190	0.184	443	152	0.34	9.9	7.5
0.4	20	6.6	5.4	12900	0.156	310	132	0.51	11.7	24.4
0.4	25	8.3	3.5	18300	0.221	410	149	0.47	14.3	27.3
0.4	30	9.9	2.4	24170	0.291	535	177	0.46	16.3	30.2

Calculation of the Modified Reynolds Number (Re_m^*) From Test Data

The modified Reynolds number (Re_m^*, equation B.1), can be calculated by knowing properties of air (the viscocity, μ), the turbine geometry (b and r_o), and the mass flow rate per disk ($\dot{m}_c$). In the data from Table B.1, the mass flow rate per disk was calculated using the scfm data taken from the air flow meter attached to the experimental set-up.

$$\mathrm{Re}_m^* = \frac{D_H \dot{m}_c}{\pi r_o^2 \mu} \tag{B.1}$$

Calculation of the Rotor Tip Mach Number (M_o)

The rotor speed (ω) was recorded using a digital tachometer. The nozzle throat temperature (T_t) in equation 3.60, B.2 was calculated using the isentropic relations for flow through a nozzle, equation B.3, assuming that the nozzle inlet conditions are the stagnation conditions and that the pressure drop is equal to the critical pressure drop.

$$M_o \equiv U_o/\sqrt{\gamma R T_t} = \frac{(P_t/P_{nt})_{crit}^{(\gamma-1)/2\gamma}}{\hat{W}_{0,r_o}+1} \tag{B.2}$$

$$T_t = T_{nt} * (P_t/P_{nt})_{crit}^{\frac{\gamma-1}{\gamma}} \tag{B.3}$$

Calulation of the Dimensionless Tangential Velocity Difference at the Rotor Inlet ($\hat{W}_o$)

Calculation of $\hat{W}_o$ (equation 3.35) is straight forward once v_θ is known at $r = r_o$. To estimate v_θ from the test data, flow is assumed to be choked whenever the pressure drop through the nozzle is larger than the critical pressure drop. Further, because the test hardware precludes direct measurement of the nozzle angle relative to the disk tangential direction, the direction of the flow out of the nozzle is assumed to be completely tangential. The velocity is then the same as the denomenator to the definition of Mo (equation B.2), or equation B.4.

$$v_\theta = \sqrt{\gamma R T_{nt} (P_t/P_{nt})_{crit}^{\frac{\gamma-1}{\gamma}}} \tag{B.4}$$

Appendix C

ANSYS Contour Plots of Velocity for 10 mm Water Turbine

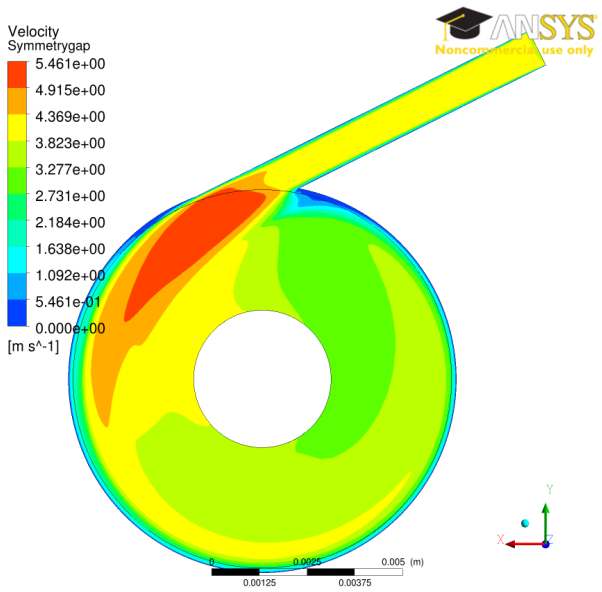

Figure C.1: Contour plot of velocity at the symmetry plane of Rotor 3, Nozzle 3 (see Table 4.2 for a full list of test parameters)

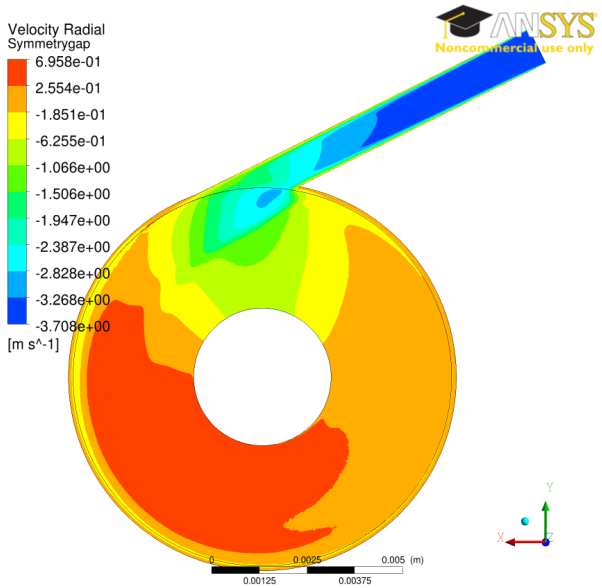

Figure C.2: Contour plot of radial velocity at the symmetry plane of Rotor 3, Nozzle 3 (see Table 4.2 for a full list of test parameters)

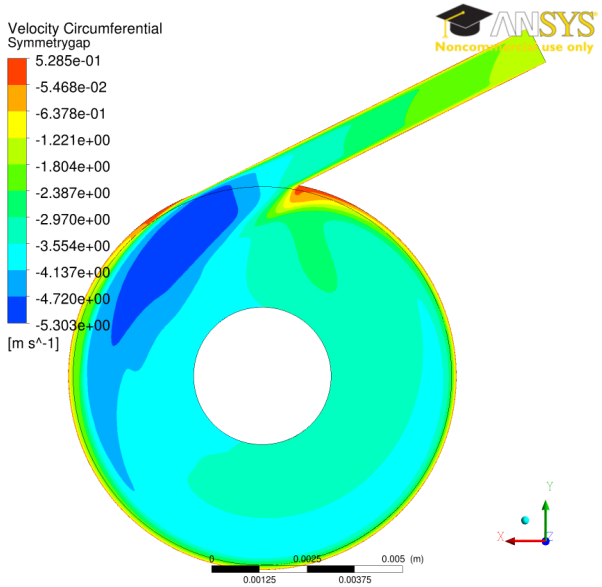

Figure C.3: Contour plot of circumferential velocity at the symmetry plane of Rotor 3, Nozzle 3 (see Table 4.2 for a full list of test parameters)

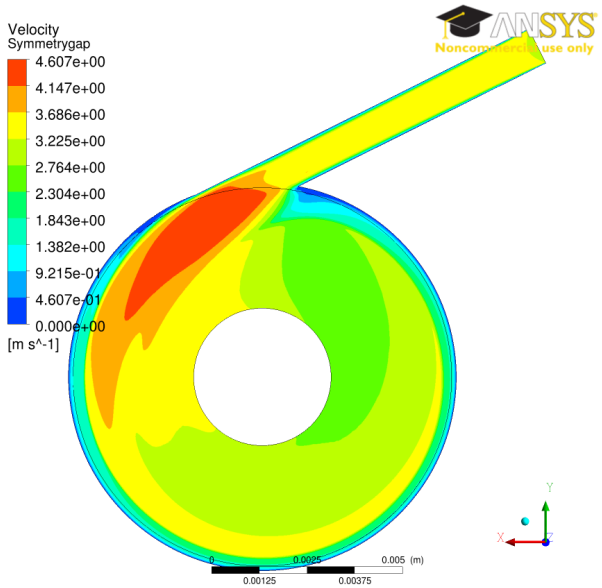

Figure C.4: Contour plot of velocity at the symmetry plane of Rotor 3, Nozzle 4 (see Table 4.2 for a full list of test parameters)

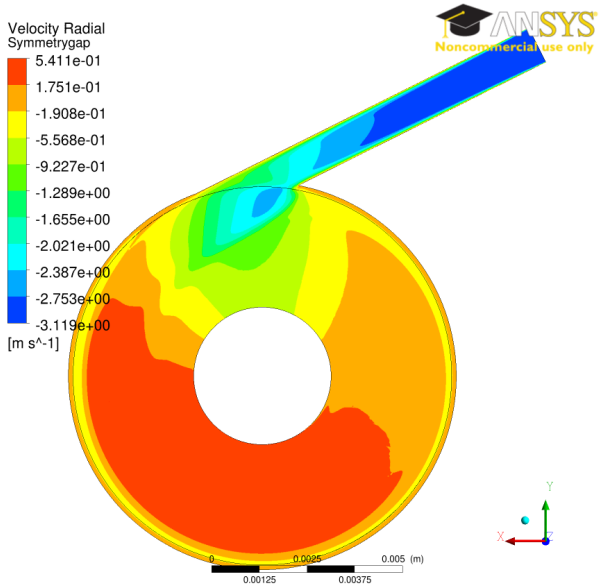

Figure C.5: Contour plot of radial velocity at the symmetry plane of Rotor 3, Nozzle 4 (see Table 4.2 for a full list of test parameters)

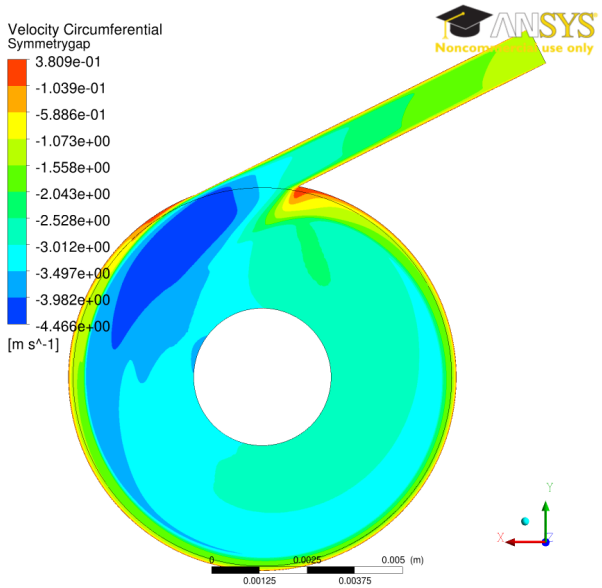

Figure C.6: Contour plot of circumferential velocity at the symmetry plane of Rotor 3, Nozzle 4 (see Table 4.2 for a full list of test parameters)

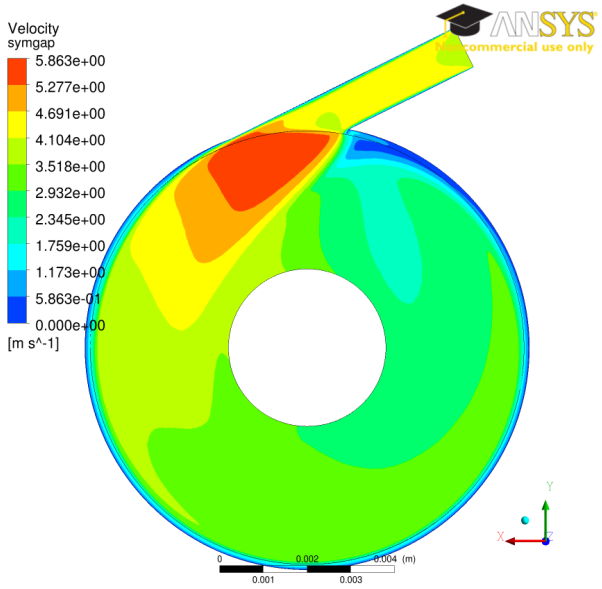

Figure C.7: Contour plot of velocity at the symmetry plane of Rotor 1, Nozzle 3 (see Table 4.2 for a full list of test parameters)

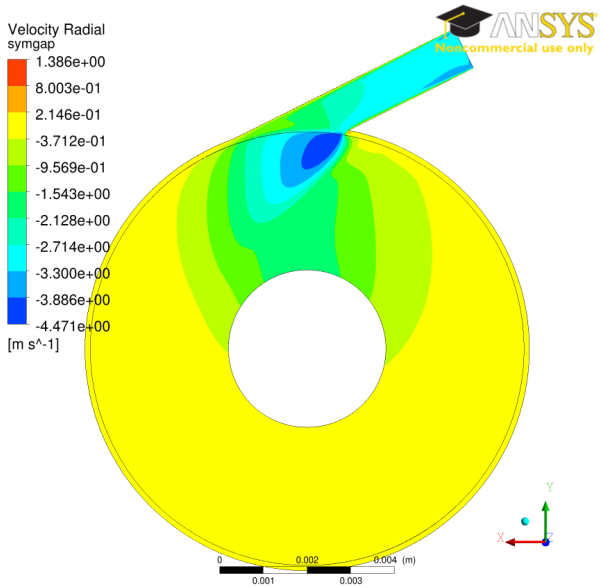

Figure C.8: Contour plot of radial velocity at the symmetry plane of Rotor 1, Nozzle 3 (see Table 4.2 for a full list of test parameters)

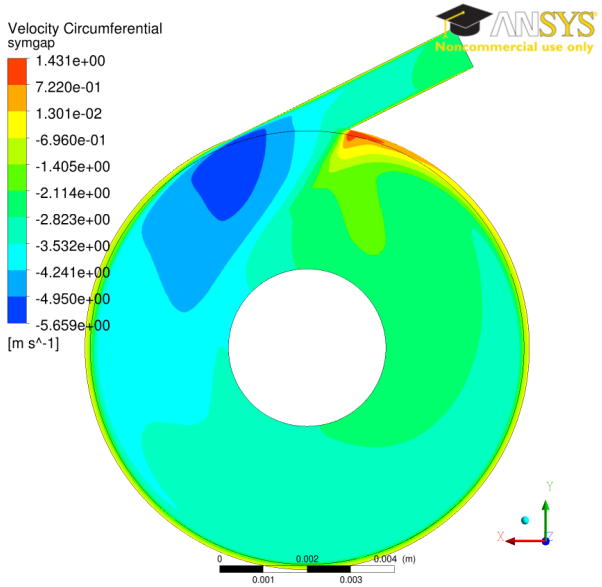

Figure C.9: Contour plot of circumferential velocity at the symmetry plane of Rotor 1, Nozzle 3 (see Table 4.2 for a full list of test parameters)

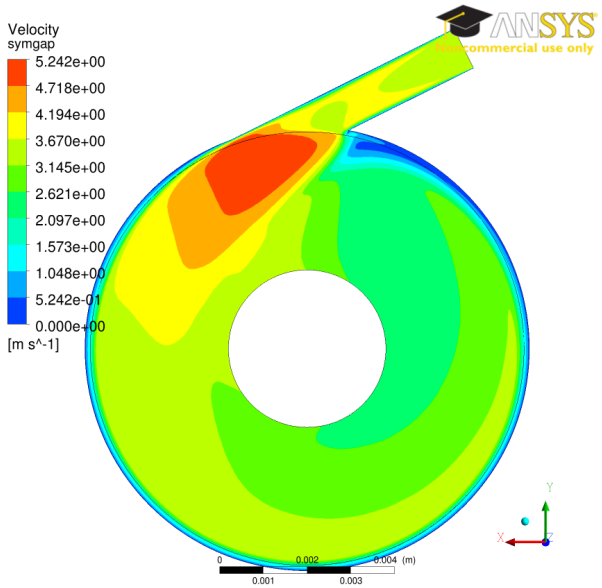

Figure C.10: Contour plot of velocity at the symmetry plane of Rotor 1, Nozzle 4 (see Table 4.2 for a full list of test parameters)

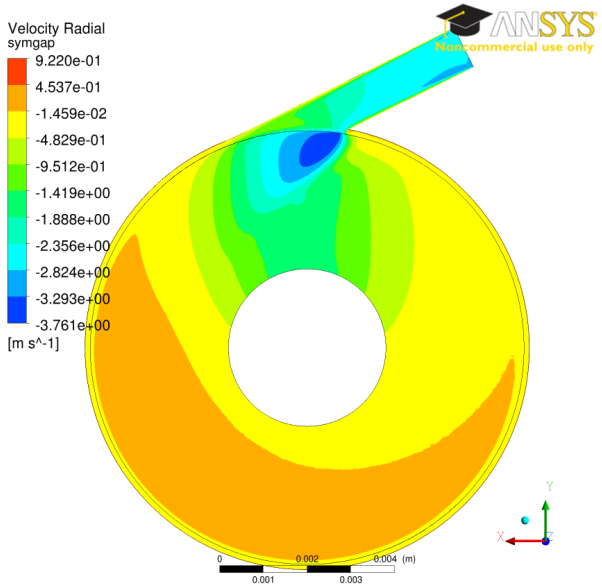

Figure C.11: Contour plot of radial velocity at the symmetry plane of Rotor 1, Nozzle 4 (see Table 4.2 for a full list of test parameters)

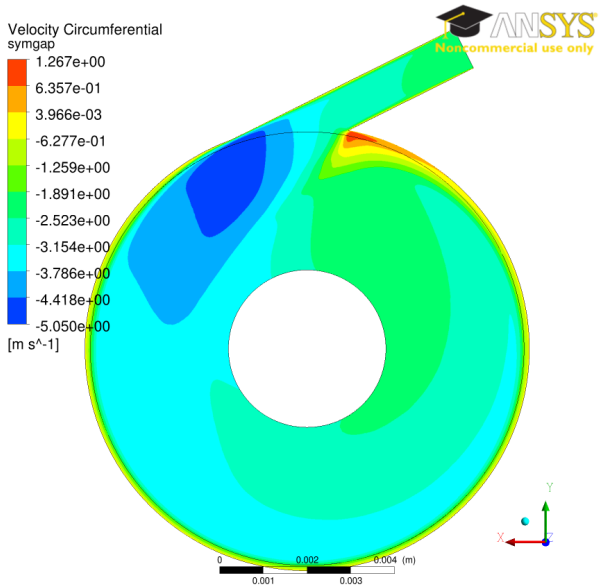

Figure C.12: Contour plot of circumferential velocity at the symmetry plane of Rotor 1, Nozzle 4 (see Table 4.2 for a full list of test parameters)

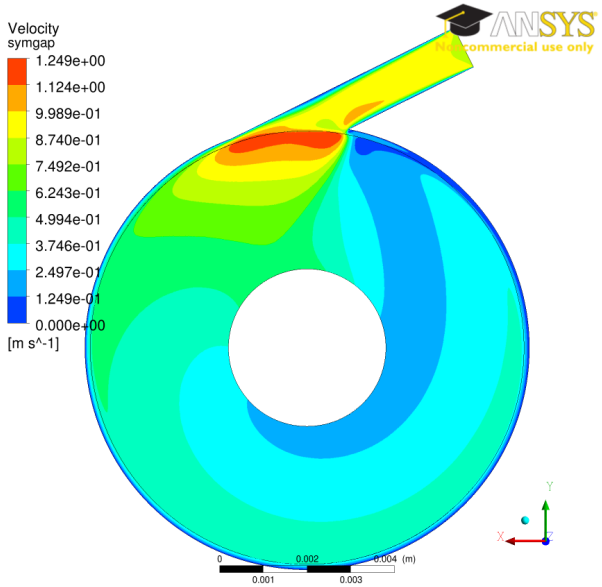

Figure C.13: Contour plot of velocity at the symmetry plane of Rotor 1, Nozzle 4 test 2 (3 g/s flow rate) (see Table 4.2 for a full list of test parameters)

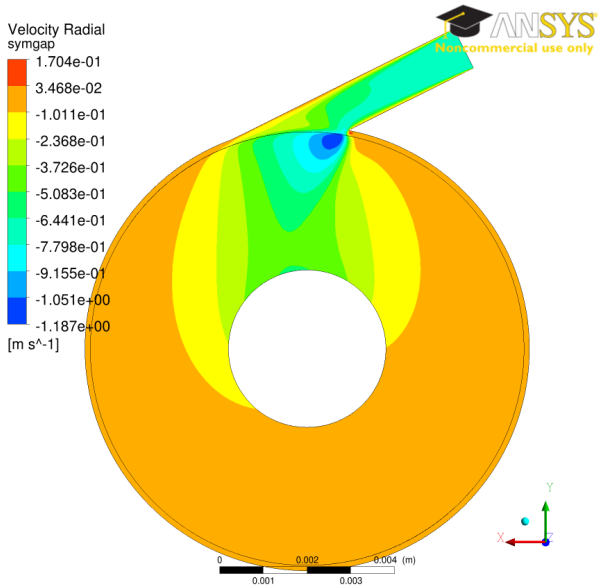

Figure C.14: Contour plot of radial velocity at the symmetry plane of Rotor 1, Nozzle 4 test 2 (3 g/s flow rate) (see Table 4.2 for a full list of test parameters)

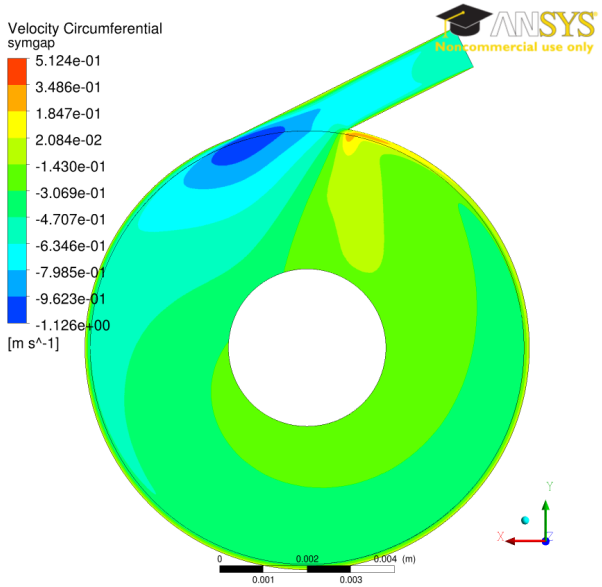

Figure C.15: Contour plot of circumferential velocity at the symmetry plane of Rotor 1, Nozzle 4 test 2 (3 g/s flow rate) (see Table 4.2 for a full list of test parameters)

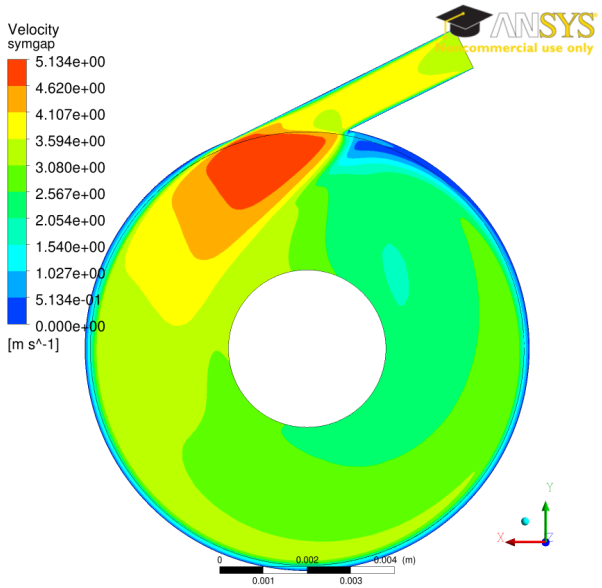

Figure C.16: Contour plot of velocity at the symmetry plane of Rotor 1, Nozzle 4 test 3 (see Table 4.2 for a full list of test parameters)

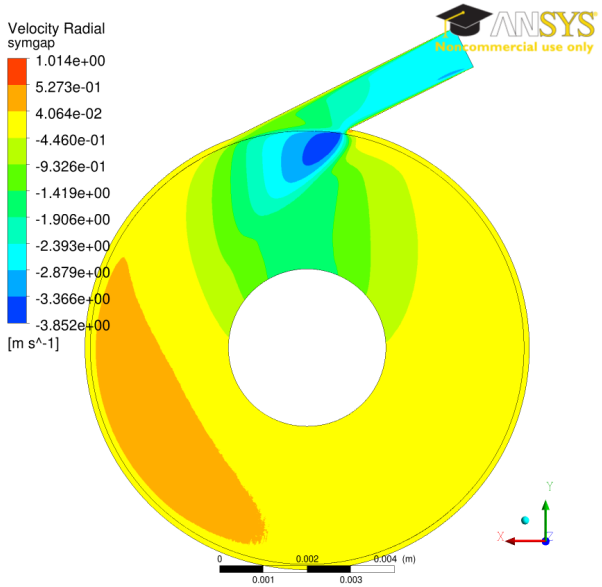

Figure C.17: Contour plot of radial velocity at the symmetry plane of Rotor 1, Nozzle 4 test 3(see Table 4.2 for a full list of test parameters)

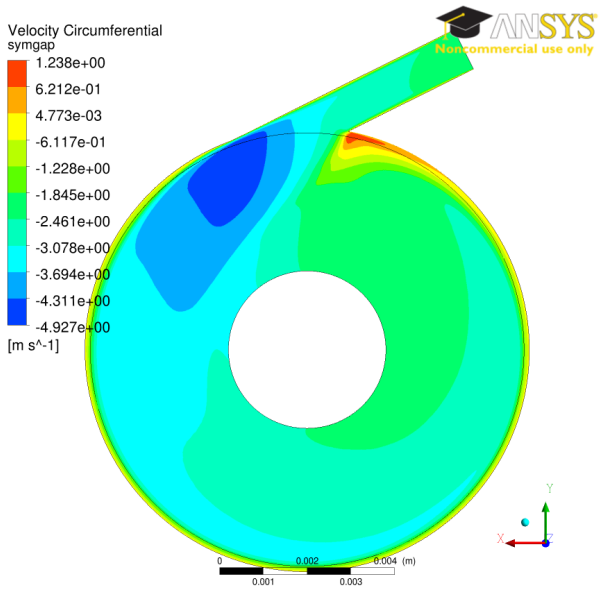

Figure C.18: Contour plot of circumferential velocity at the symmetry plane of Rotor 1, Nozzle 4 test 3 (see Table 4.2 for a full list of test parameters)

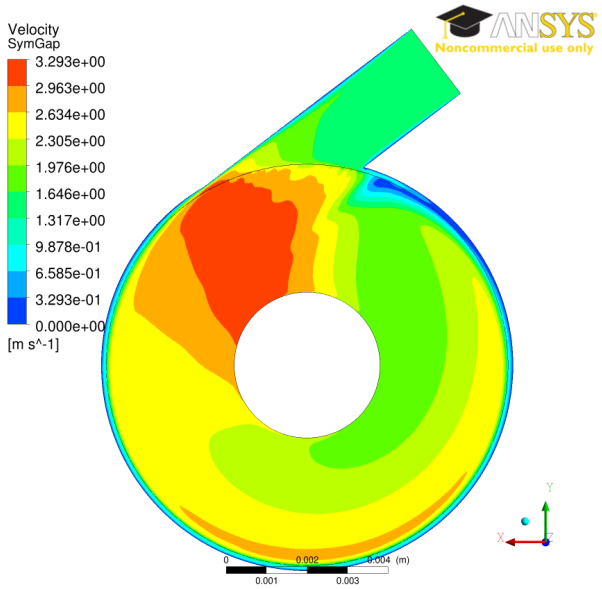

Figure C.19: Contour plot of velocity at the symmetry plane of Rotor 1, Nozzle 7 (see Table 4.2 for a full list of test parameters)

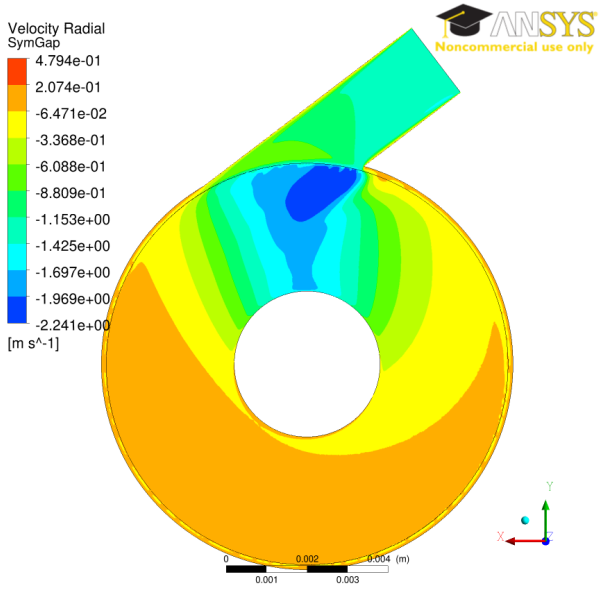

Figure C.20: Contour plot of radial velocity at the symmetry plane of Rotor 1, Nozzle 7 (see Table 4.2 for a full list of test parameters)

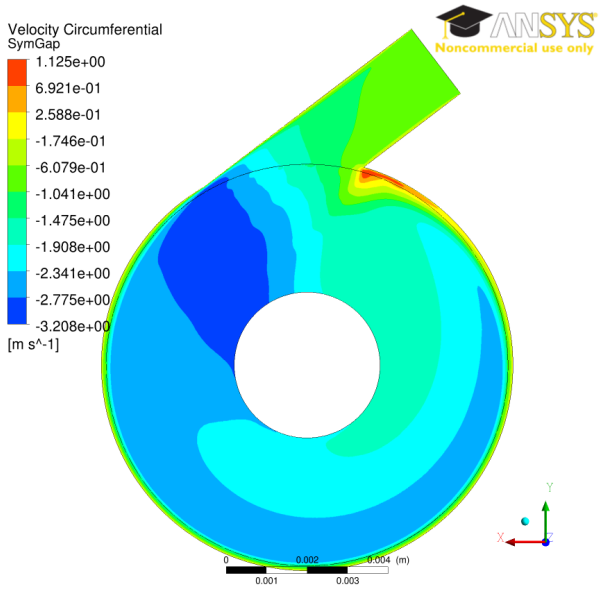

Figure C.21: Contour plot of circumferential velocity at the symmetry plane of Rotor 1, Nozzle 7 (see Table 4.2 for a full list of test parameters)

Bibliography

[1] M. C. Breiter and K. Pohlhausen. *Laminar Flow Between Two Parallel Rotating Disks*. Tech. rep. ARL 62-318. Aeronautical Research Laboratories, Wright-patterson Air Force Base, Ohio, 1962.

[2] V. Carey. "Assessment of Tesla Turbine Performance for Small Scale Rankine Combined Heat and Power Systems". In: *Journal of Engineering for Gas Turbines and Power* 132.12, 122301 (2010), p. 122301. DOI: 10.1115/1.4001356.

[3] *Combined Heat and Power*. Tech. rep. International Energy Agency, 2008. URL: http://www.iea.org/media/files/chp/chp_report.pdf.

[4] G. Croce, P. D'agaro, and C. Nonino. "Three-dimensional roughness effect on microchannel heat transfer and pressure drop". In: *International Journal of Heat and Mass Transfer* 50.25-26 (Dec. 2007), pp. 5249–5259. ISSN: 0017-9310.

[5] R. T. Deam et al. "On Scaling Down Turbines to Millimeter Size". In: *Journal of Engineering for Gas Turbines and Power* 130.5 (2008), pp. 052301–9. DOI: 10.1115/1.2938516.

[6] Energy and Environmental Analysis (an ICF International Company). *Technology Characterization: Microturbines*. Tech. rep. Prepared for Environmental Protection Agency, 2008. URL: www.epa.gov/chp/documents/catalog_chptech_microturbines.pdf.

[7] Alan H. Epstein. "Millimeter-Scale, Micro-Electro-Mechanical Systems Gas Turbine Engines". In: *Journal of Engineering for Gas Turbines and Power* 126.2 (2004), pp. 205–226. DOI: 10.1115/1.1739245. URL: http://link.aip.org/link/?GTP/126/205/1.

[8] A. Carlos Fernandez-Pello. "Micropower generation using combustion: Issues and approaches". In: *Proceedings of the Combustion Institute* 29.1 (2002), pp. 883 –899. ISSN: 1540-7489. DOI: 10.1016/S1540-7489(02)80113-4. URL: http://www.sciencedirect.com/science/article/pii/S1540748902801134.

[9] Kelvin Fu et al. "Design and Experimental Results of Small-Scale Rotary Engines". In: *ASME Conference Proceedings* IMECE2001/MEMS-23924 (2001).

[10] G. Gamrat et al. "An Experimental Study and Modelling of Roughness Effects on Laminar Flow in Microchannels". In: *Journal of Fluid Mechanics* 594.-1 (2008), pp. 399–423. DOI: 10.1017/S0022112007009111.

[11] A. Guha and B. Smiley. "Experiment and analysis for an improved design of the inlet and nozzle in Tesla disc turbines". In: *Proceedings of the Institution of Mechanical Engineers, Part A: Journal of Power and Energy* 224.2 (2010), pp. 261–277. ISSN: 0957-6509. DOI: 10.1243/09576509JPE818.

[12] G. P. Hoya and A. Guha. "The design of a test rig and study of the performance and efficiency of a Tesla disc turbine". In: *Proceedings of the Institution of Mechanical Engineers, Part A: Journal of Power and Energy* 223.4 (2009), pp. 451–465. ISSN: 0957-6509. DOI: 10.1243/09576509JPE664.

[13] S. G. Kandlikar et al. "Characterization of surface roughness effects on pressure drop in single-phase flow in minichannels". In: *Physics of Fluids* 17.10 (2005), p. 100606. ISSN: 10706631. DOI: 10.1063/1.1896985.

[14] Vedavalli G. Krishnan, Zohora Iqbal, and Michel M. Maharbiz. "A Micro Tesla Turbine for Power Generation from Low Pressure Heads and Evaporation Driven Flows". In: *Solid-State Sensors, Actuators and Microsystems Conference (TRANSDUCERS), 2011 16th International* (2011), pp. 1851 –1854. DOI: 10.1109/TRANSDUCERS.2011.59698789.

[15] B. R. Munson, D. F. Young, and T. H. Okiishi. *Fundamentals of Fluid Mechanics*. 5th ed. New York: Wiley, 2006. ISBN: 0471675822 9780471675822.

[16] P.A. Pilavachi. "Mini- and micro-gas turbines for combined heat and power". In: *Applied Thermal Engineering* 22.18 (2002), pp. 2003 –2014. ISSN: 1359-4311. DOI: 10.1016/S1359-4311(02)00132-1. URL: http://www.sciencedirect.com/science/article/pii/S1359431102001321.

[17] W. Rice. "An Analytical and Experimental Investigation of Multiple Disk Turbines". In: *Journal of Engineering for Power* (Jan. 1965), pp. 29–36.

[18] V. Romanin and V. Carey. "Strategies for Performance Enhancement of Tesla Turbines for Combined Heat and Power Applications". In: *Paper no. ES2010-90251, ASME Energy and Sustainability Conference Proceedings* 2.43956 (2010), pp. 57–64.

[19] Vince D. Romanin. "Strategies for performance enhancements of Tesla turbines for combined heat and power applications". MA thesis. U.C. Berkeley, May 2010.

[20] Vince D. Romanin and Van P. Carey. "An integral perturbation model of flow and momentum transport in rotating microchannels with smooth or microstructured wall surfaces". In: *Physics of Fluids* 23.8, 082003 (2011), p. 082003. DOI: 10.1063/1.3624599. URL: http://link.aip.org/link/?PHF/23/082003/1.

[21] N. Tesla. "Turbine". In: *US Patent No. 1,061,206* (May 1913).